Wind-Driven Processes Controlling Oceanic Heat Delivery to the Amundsen Sea, Antarctica

Tiago S. Dotto,[a] Alberto C. Naveira Garabato,[a] Sheldon Bacon,[b] Paul R. Holland,[c] Satoshi Kimura,[d] Yvonne L. Firing,[b] Michel Tsamados,[e] Anna K. Wåhlin,[f] and Adrian Jenkins[c]

[a] *Ocean and Earth Science, University of Southampton, Southampton, United Kingdom*
[b] *National Oceanography Centre, Southampton, United Kingdom*
[c] *British Antarctic Survey, Cambridge, United Kingdom*
[d] *Japan Agency for Marine-Earth Science and Technology, Yokosuka, Japan*
[e] *Centre for Polar Observation and Modelling, University College London, London, United Kingdom*
[f] *Department of Marine Sciences, University of Gothenburg, Gothenburg, Sweden*

ABSTRACT

Variability in the heat delivery by Circumpolar Deep Water (CDW) is responsible for modulating the basal melting of the Amundsen Sea ice shelves. However, the mechanisms controlling the CDW inflow to the region's continental shelf remain little understood. Here, a high-resolution regional model is used to assess the processes governing heat delivery to the Amundsen Sea. The key mechanisms are identified by decomposing CDW temperature variability into two components associated with 1) changes in the depth of isopycnals [heave (HVE)], and 2) changes in the temperature of isopycnals [water mass property changes (WMP)]. In the Dotson–Getz trough, CDW temperature variability is primarily associated with WMP. The deeper thermocline and shallower shelf break hinder CDW access to that trough, and CDW inflow is regulated by the uplift of isopycnals at the shelf break—which is itself controlled by wind-driven variations in the speed of an undercurrent flowing eastward along the continental slope. In contrast, CDW temperature variability in the Pine Island–Thwaites trough is mainly linked to HVE. The shallower thermocline and deeper shelf break there permit CDW to persistently access the continental shelf. CDW temperature in the area responds to wind-driven modulation of the water mass on-shelf volume by changes in the rate of inflow across the shelf break and in Ekman pumping-induced vertical displacement of isopycnals within the shelf. The western and eastern Amundsen Sea thus represent distinct regimes, in which wind forcing governs CDW-mediated heat delivery via different dynamics.

1. Introduction

The West Antarctic Ice Sheet has undergone intense mass loss since at least the 1990s (Paolo et al. 2015; Shepherd et al. 2018), driven mainly by the acceleration of outlet glaciers associated with thinning of the floating ice shelves (Pritchard et al. 2012; Dutrieux et al. 2014). In the South Pacific, branches of the Antarctic Circumpolar Current (ACC) carrying warm Circumpolar Deep Water (CDW) veer southward, reaching the Antarctic continental slope around 100°W (Orsi et al. 1995; Walker et al. 2013). Troughs cutting across the continental shelf provide direct routes by which this CDW, or its slightly colder modified varieties, gain access to the coastal areas (Wåhlin et al. 2010; Jacobs et al. 2011; St-Laurent et al. 2013), bringing heat and thus contributing significantly to the ice shelves' thinning (Paolo et al. 2015; Christianson et al. 2016; Jenkins et al. 2018).

In the Amundsen Sea (Fig. 1a), warm (2°–4°C above the in situ freezing temperature) and saline deep waters are observed throughout the year within the Dotson–Getz and Pine Island–Thwaites troughs (Wåhlin et al. 2013; Mallett et al. 2018). Within each trough, a cyclonic circulation effects an inflow of CDW along the channel's

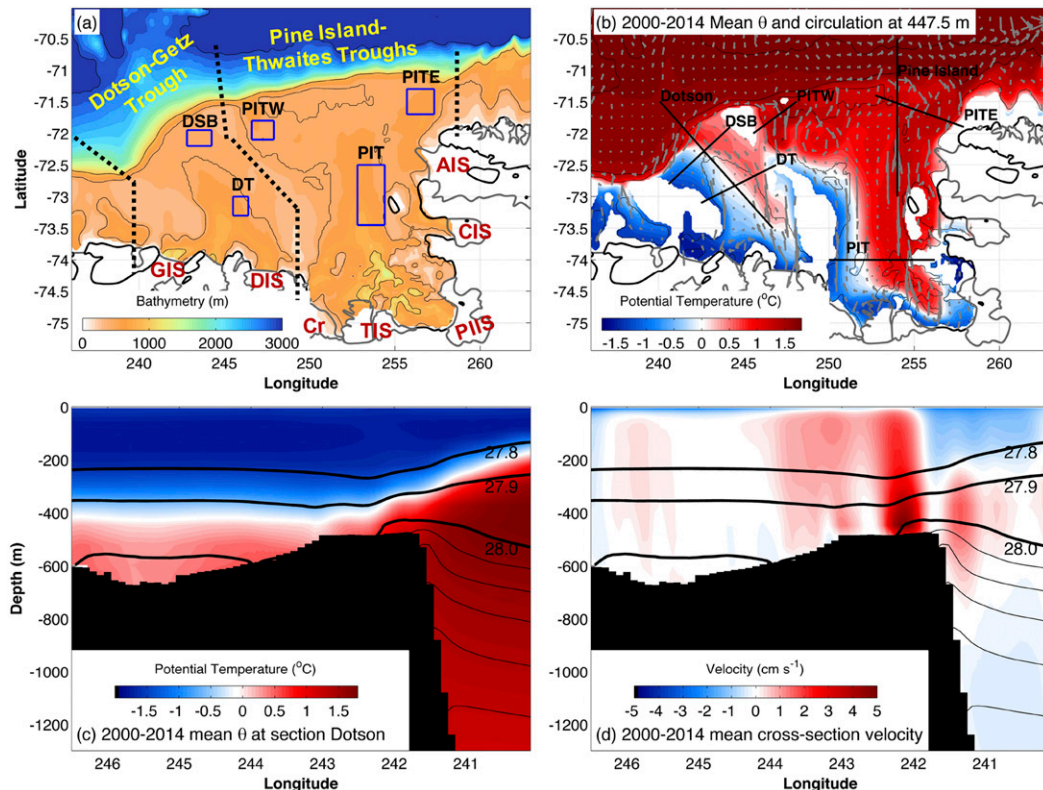*Corresponding author*: Tiago S. Dotto, tiagosdotto@gmail.com

FIG. 1. (a) Amundsen Sea bathymetry in the model. Dotted lines show the definition of the Dotson–Getz trough and the Pine Island–Thwaites troughs used in this work. Blue rectangles indicate the areas used to analyze the decomposition of potential temperature θ, labeled Dotson Shelf Break (DSB), Inner Dotson Trough (DT), Pine Island–Thwaites (PIT) trough, Pine Island–Thwaites West (PITW) trough, and Pine Island–Thwaites East (PITE) trough. Isobaths of 500, 1000 and 3000 m are depicted. Local ice shelves are labeled: Abbot Ice Shelf (AIS), Cosgrove Ice Shelf (CIS), Pine Island Ice Shelf (PIIS), Thwaites Ice Shelf (TIS), Crosson Ice Shelf (Cr), Dotson Ice Shelf (DIS), and Getz Ice Shelf (GIS). (b) The 2000–14 time-mean θ (color) and horizontal velocity (vectors plotted every six grid cells) near 450-m depth. The map shows the location of the sections used to evaluate the model. The labels follow the areas in (a). Along-trough sections are labeled Dotson and Pine Island. (c) The 2000–14 time-mean θ (color) overlaid by neutral density γ^n surfaces along the Dotson Trough. Isopycnals $> 28.0 \, \text{kg m}^{-3}$ (thin black lines) are spaced every 0.02 kg m^{-3}. (d) As in (c), but for time-mean cross-section velocity (positive values are northeastward).

eastern flank and an outflow of colder and fresher CDW along the western flank (Fig. 1b), following interaction with the ice shelves (Schodlok et al. 2012; Nakayama et al. 2013; Assmann et al. 2013; Ha et al. 2014; Kalén et al. 2016; Gourmelen et al. 2017; Mallett et al. 2018). Estimates using in situ data indicate oceanic heat transports of 1–3 TW through the Dotson–Getz and Pine Island–Thwaites troughs, corresponding to ice melt rates of ~100–300 km^3 yr^{-1} (Walker et al. 2007; Wåhlin et al. 2010; Ha et al. 2014). Daily-to-decadal variability in the inflowing CDW and in the heat content of the Amundsen Sea have been observed (Jacobs et al. 2011; Wåhlin et al. 2013; Dutrieux et al. 2014; Jenkins et al. 2018).

Different processes have been suggested to govern the CDW inflow to the continental shelves, involving wind forcing, ocean dynamics, and flow–topography interactions. Wind forcing, the variability of which is influenced by atmospheric teleconnections with the tropics, has been shown to correlate with the thickness of the CDW layer in the Amundsen Sea (Thoma et al. 2008; Steig et al. 2012; Dutrieux et al. 2014) and with the velocity of the inflowing transport within the troughs (Assmann et al. 2013; Wåhlin et al. 2013). Generally, larger inflow of CDW onto the continental shelf is associated with periods of intensified eastward winds, although the controlling dynamics remain unclear (Thoma et al. 2008). Wind perturbations have been shown to force barotropic fluctuations in the on-shelf ocean circulation (Assmann et al. 2013; Wåhlin et al. 2013; Kalén et al. 2016). However, the variability in along-shelf-break wind stress exhibits a poor relationship with

temperature (Wåhlin et al. 2013), suggesting that other mechanisms regulate temperature variations within the troughs. Recent studies have pointed to Ekman suction at the shelf break as a significant driver of temperature changes in the inner Amundsen Sea (Kim et al. 2017; Webber et al. 2019).

Ocean dynamics provide other candidate mechanisms for controlling the region's heat content. Walker et al. (2013) argued that an eastward slope undercurrent—found under the westward surface current—advects warm waters onto the shelf. The undercurrent flows along the continental slope, but can cross the shelf break when it encounters a trough (Klinck 1996; Assmann et al. 2013; St-Laurent et al. 2013). The associated circulation may inject the CDW that floods the trough (Walker et al. 2013). Another proposed mechanism focusses on the on-shelf bottom Ekman transport (Wåhlin et al. 2012). Under an eastward slope current, such as observed in the eastern Amundsen Sea, the bottom Ekman transport is upslope and toward the shelf, and may thus provide a continuous source of heat to the shelf via uplifting of waters lying at a depth of ~800 m offshore (Wåhlin et al. 2012). Eddies and tides have also been argued to mediate the on-shelf heat transport elsewhere around Antarctica (Martinson and McKee 2012; Thompson et al. 2014; Rodriguez et al. 2016; Paloczy et al. 2018; Stewart et al. 2018), although the importance of these processes in the Amundsen Sea is less clear.

More recently, changes in the remote sources of CDW have been proposed to play a significant role in the variability of the Amundsen Sea heat content. Nakayama et al. (2018) suggested that the offshore CDW characteristics advected from afar, that is, by the large-scale ocean circulation, might be as important as regional atmospheric forcing in setting the temperature variability on the Amundsen Sea continental shelf. Further, barotropic Kelvin waves, generated by wind forcing elsewhere around Antarctica and propagating along continental margins, have been indicated as a possible regulator of oceanic heat content off West Antarctica (Spence et al. 2017; Webb et al. 2019), with consequences for coastal temperatures in future wind-changing scenarios (Spence et al. 2014).

In summary, it is important to identify the mechanisms behind the variability of the CDW inflow to the Amundsen Sea continental shelf, in order to project how future changes in regional oceanic conditions will impact the evolution of the ice shelves downstream (e.g., Christianson et al. 2016; Gourmelen et al. 2017; Jenkins et al. 2018). Generally, most studies agree that the heat content of the Amundsen Sea is related to the wind speed and direction, but a variety of controlling processes have

been proposed in the same or different parts of the region, thereby generating a blurred picture of the key governing mechanisms. Here, we add clarity to this picture, by (i) evaluating the mechanisms through which wind regulates the oceanic heat delivery to the Amundsen Sea in a high-resolution numerical model, and (ii) assessing the dynamics involved in each mechanism. The paper is organized as follows: section 2 provides a description of the model outputs, and of the methods used; section 3 presents the main results on the driving forces of CDW flow into the troughs; and sections 4 and 5 provide a discussion and the main conclusions, respectively.

2. Data and methods

a. Ocean circulation model

We employed monthly mean outputs of the ocean circulation model of Kimura et al. (2017). Briefly, the simulation is based on the Massachusetts Institute of Technology general circulation model (MITgcm) adapted to include sub-ice-shelf cavities (Losch 2008) and coupled with a sea ice model based on a viscous-plastic rheology (Losch et al. 2010). The ocean model solves the hydrostatic Boussinesq momentum equations and advection–diffusion equations for temperature and salinity on a generalized curvilinear Arakawa C-grid, using the finite-volume method and z levels in the vertical (Marshall et al. 1997). The model domain covers the Amundsen Sea between 75.5° and 62°S and between 80° and 140°W, and includes eight sub-ice-shelf cavities (Getz, Dotson, Crosson, Thwaites, Pine Island, Cosgrove, Abbot, and Venable). In this study, we focus on the processes happening on the continental shelf to the north of Dotson–Getz and Pine Island–Thwaites (Fig. 1a). The model's horizontal resolution ranges from 2.8 km in the south of the domain to 5.2 km in the north. Vertically, it has 50 z levels with spacing ranging from 10 m at the surface to 200 m near the bottom (50–80 m on the deeper parts of the continental shelf and the slope). The vertical diffusion is represented using the K-profile parameterization (Large et al. 1994), and there is no explicit horizontal diffusion for temperature and salinity. The model does not include tidal forcing. Seabed and ice-shelf topography are from the global 1-min Refined Topography dataset (Timmermann et al. 2010).

The initial conditions are based on the *World Ocean Atlas 2009* (Antonov et al. 2010; Locarnini et al. 2010). Velocity, temperature, and salinity at the boundaries are set to steady climatological fields from the Southern Ocean model in Holland et al. (2014). Atmospheric forcing is from ERA-Interim (Dee et al. 2011), and consists of zonal and meridional 10-m winds, 2-m air temperature and specific humidity, downward shortwave and
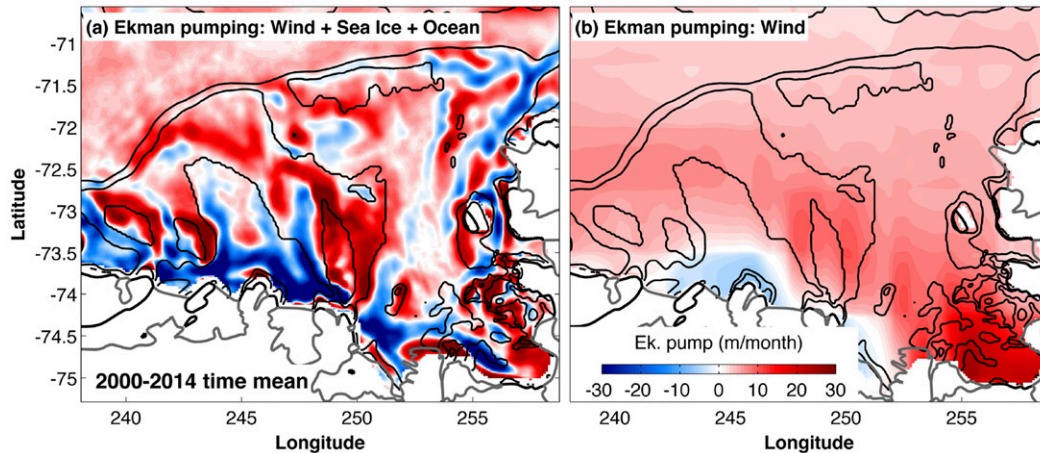
FIG. 2. The 2000–14 time-mean (a) Ekman pumping velocity (positive upward) using the combined wind + sea ice + ocean current stress and (b) Ekman pumping velocity using wind stress only. Isobaths of 500, 1000, and 3000 m are depicted.

longwave radiation, and precipitation. MITgcm can provide the ocean surface stress diagnostic output as a wind-only stress or as a coupling of the wind, sea ice drift and ocean current stresses weighted by the sea ice concentration in polar regions. The latter is the effective stress that is used by the model and is considered in the present work. The vertical Ekman pumping velocity w_E is calculated from the monthly mean outputs as

$$w_E = \frac{\nabla \times \boldsymbol{\tau}}{\rho_0 f}, \tag{1}$$

where seawater density ρ_0 is $1028 \, \mathrm{kg \, m^{-3}}$, the Coriolis parameter f is $-1.38 \times 10^{-4} \, \mathrm{s^{-1}}$, and $\nabla \times \boldsymbol{\tau}$ is the ocean surface stress curl. The calculation was repeated for the wind-only stress curl. Although the large-scale patterns of wind stress and ocean surface stress resemble each other, the coupled stress produces strong, localized features (Fig. 2a) that are not observed in the wind-only stress (Fig. 2b). The coupled stress captures a more accurate picture of the real stress and its association with the ocean, particularly in ice-covered areas (e.g., Kimura et al. 2017; Dewey et al. 2018; Meneghello et al. 2018).

The model was run from January 1991 to December 2014 and was spun up after 1994 (Kimura et al. 2017). We focus our analysis in the post-2000 period, because the model simulated unrealistic deep convection in the Amundsen Sea between 1997 and 2001 (see, for instance, Fig. 7a of Kimura et al. 2017). Nevertheless, including earlier years does not alter qualitatively the main results of this work (not shown). Trends were removed before all the analyses; mean seasonal cycles are retained, unless otherwise specified.

The model has been validated (see supplemental material and Kimura et al. 2017) and shown to be able to represent well many aspects of the Amundsen Sea circulation, sea ice cover, and dynamical relationships between the ocean circulation and wind forcing. The water mass structure (Figs. S2–S4 in the online supplemental material), the average deep circulation including the main warm water pathways onto the shelf along the troughs' eastern flanks (Fig. 1b), the flooding of the troughs with CDW-derived water masses (Fig. 1c), and the velocity structure at the slope (Fig. 1d and Fig. S5) are all in qualitative agreement with in situ data (Wåhlin et al. 2013; Walker et al. 2013). The seasonality of CDW properties within the troughs and their interannual changes off Pine Island Glacier qualitatively agree with observations (Dutrieux et al. 2014; Mallett et al. 2018). The model also agrees with observations of the ice shelves' basal melting rates (see Kimura et al. 2017) and, qualitatively, with the observed decadal fluctuations in the deep temperature of the Amundsen Sea continental shelf (e.g., Dutrieux et al. 2014; Jenkins et al. 2016, 2018). Quantitatively, the model displays several biases in water mass properties (e.g., upper layers are generally saltier and warmer than in observations, except in the Pine Island–Thwaites subdomain; Figs. S3, S4) and in the velocity of the currents inflowing the troughs, which is weaker than in situ estimates (Fig. S5). The reader is referred to the supplemental material for a thorough evaluation of the model and its biases.

b. Heave and isopycnal property decomposition

The partitioning of potential temperature θ changes into isopycnal property (i.e., temperature changes along

isopycnal surfaces) and heave-driven (i.e., associated with a vertical displacement of isopycnal surfaces) components was introduced by Bindoff and McDougall (1994), and is useful to analyze temporal changes of water masses (e.g., Desbruyères et al. 2017; Firing et al. 2017). Although displacements of isopycnals are not necessarily purely adiabatic (e.g., Desbruyères et al. 2017), the decomposition points to the relative contributions to temperature changes in the water column of diabatic processes (e.g., changes in buoyancy fluxes or lateral advection of new water masses) and adiabatic displacements in the water column (e.g., due to wind-driven vertical motion). Equation (2) shows the terms involved in the calculation:

$$\Delta\theta|_z \simeq \Delta\theta|_{\gamma^n} - \Delta z|_{\gamma^n} \overline{\frac{\partial\theta}{\partial z}}, \qquad (2)$$

where $\Delta\theta$ (Δz) represents the temporal deviation from the 2000–14 time-mean θ (depth), and $|_z$ and $|_{\gamma^n}$ indicate the evaluation of a variable on depth z (defined to be positive upward and set to zero at the mean sea level) and neutral density γ^n levels, respectively. Thus, the decomposed values are anomalies relative to the 2000–14 mean. The calculation uses monthly mean outputs. For the calculation of the right-hand side terms in Eq. (2), θ values are first binned onto γ^n levels (set to 26.50–28.28 kg m^{-3} every 0.01 kg m^{-3}, refined to 0.002 kg m^{-3} between 27.00 and 27.80 kg m^{-3} and to 0.001 kg m^{-3} between 27.80 and 28.10 kg m^{-3}) and vertical gaps are filled by linear interpolation. The $\overline{\partial\theta/\partial z}$ term is the 2000–14 averaged vertical gradient of θ. After calculating each term, it is binned back to the model's depth levels, and vertical gaps are linearly interpolated.

The first term on the right-hand side of Eq. (2) represents θ changes on isopycnals and is associated with changes in water mass properties (WMP). The second term on the right-hand side represents changes in θ due to vertical displacements of isopycnals, or heave (HVE), and is likely to be associated with dynamical variability. WMP represents a shift in the θ–salinity space at constant density and therefore involves a compensating change in salinity, whereas in HVE the density is altered due to changes in θ and salinity corresponding to the background stratification (Bindoff and McDougall 1994). The sum of all terms in Eq. (2) can give a nonnegligible residual at depths with large vertical θ gradient (e.g., the thermocline) or exposed to air–ice–ocean interactions. Thus, our main focus is on depths > 300 m, which is the depth range where the CDW-derived waters ($\theta > 0°$C) are found on the Amundsen Sea continental shelf (Jacobs et al. 2011;

Wåhlin et al. 2013; Mallett et al. 2018). The estimated rate of change of a variable between different months, that is, $\partial P/\partial t$, where P is the variable (e.g., θ or the depth of an isopycnal), is evaluated using centered differences (e.g., the difference between March and January represents the characteristic change in February).

c. Cross-section velocity and transport calculation

Observations have suggested that an undercurrent flowing along the continental slope in the Amundsen Sea is important to the heat advection into the troughs (e.g., Walker et al. 2013). To represent variations in the strength of the circulation on the continental shelf and slope, we defined a metric that reflects the undercurrent strength as the monthly maximum cross-section velocity directed southward (or eastward for the sections crossing the slope) below 200 m (see Fig. 1b for the location of sections analyzed). To distinguish the eastward undercurrent flowing along the shelf break and continental slope from the southward flow within the troughs, the latter is defined hereafter as "bottom-enhanced southern flow." Results are consistent if the mean velocity is used instead, but the maximum velocity reflects better the speed of the undercurrent's core (e.g., Walker et al. 2013). Cross-section transport is calculated at sections Pine Island–Thwaites East (PITE) and West (PITW), which are important sources of CDW to the inner Pine Island–Thwaites (PIT) trough (Fig. 1b; Nakayama et al. 2013). The poleward cross-section velocity is integrated along the section and from the ocean floor to the 28.00 kg m^{-3} isopycnal (i.e., the upper limit of the CDW layer) using the monthly mean outputs:

$$\text{Transport} = \int_{H}^{h_{28}} \int_{0}^{x} u_r \, dx \, dz \quad \begin{cases} u_r \times 1, & u_r \geq 0 \\ u_r \times 0, & |u_r < 0 \end{cases}, \quad (3)$$

where H is the local ocean depth; h_{28} is the depth of the 28.00 kg m^{-3} isopycnal; x is the along-section distance; and u_r is the poleward cross-section velocity (oriented 100° clockwise of zonal direction in the PITE, and 50° in the PITW, to match the trough orientation—positive values indicate southward flow). Note that areas of northward flow are omitted from Eq. (3).

To contrast different oceanic and climatic conditions in the Amundsen Sea embayment, composites of a variable of the model are created by averaging it over times when a given property is less than its 20th percentile or greater than its 80th percentile. Results are not qualitatively sensitive to changing the percentile thresholds to 20 ± 10 or 80 ± 10.
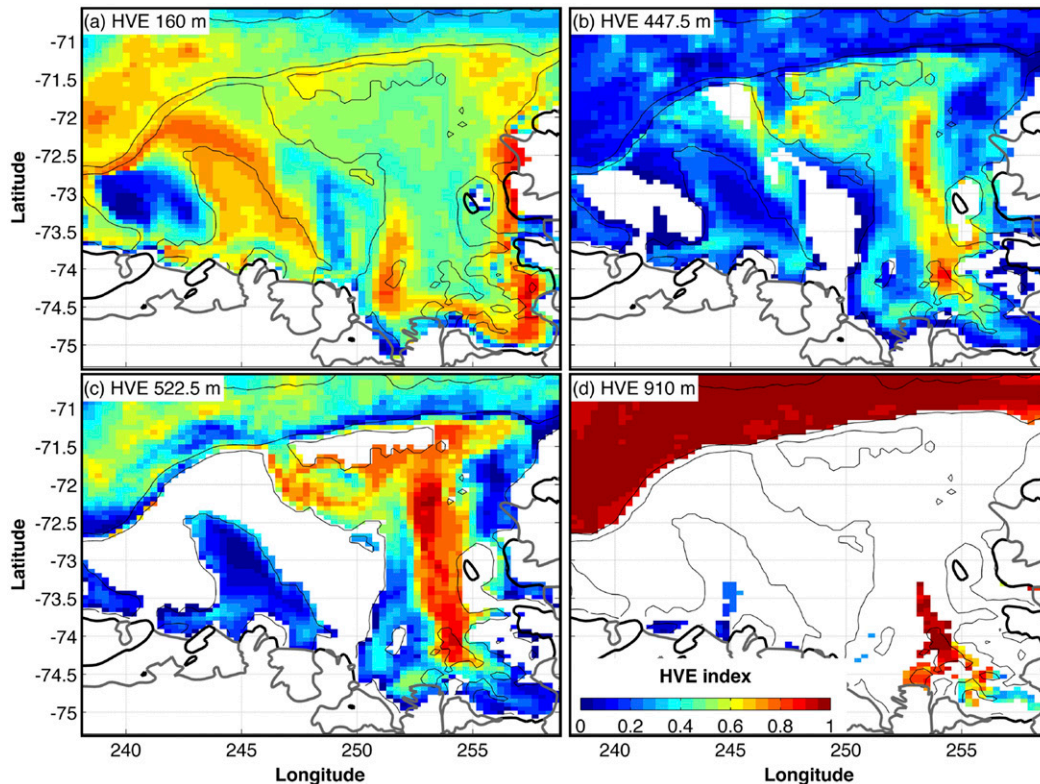
FIG. 3. Relative contribution of heave component (HVE index) to detrended temperature variance for the period 2000–14, at different depths (indicated in the upper-left corner of each panel). A value of 1 represents purely heave-driven temperature variability (HVE), and 0 exactly compensating changes in temperature and salinity on isopycnals (WMP). Isobaths of 500, 1000, and 3000 m are depicted by the thin black lines.

3. Results

In the next subsections, we first define an index to categorize the relative importance of contributions associated with HVE and with WMP to the temperature variations ($\Delta\theta$) in the Amundsen Sea continental shelf. The driving forces that lead to each mechanism are subsequently investigated.

a. Heave versus isopycnal property changes

We express the relative importance of the HVE and WMP contributions to the reconstructed $\Delta\theta$ for each model grid point in the Amundsen Sea by defining the ratio of the sum over time of the squared HVE component divided by the sum of the squared reconstructed $\Delta\theta$ (i.e., the fraction of the variance in detrended monthly $\Delta\theta$ that can be explained by heaving), such as

$$\text{HVE index} = \frac{\sum \text{HVE}^2}{\sum(\text{HVE}^2 + \text{WMP}^2)}. \qquad (4)$$

The reconstruction [right-hand side of Eq. (2)] closely follows $\Delta\theta$ [left-hand side of Eq. (2)], particularly for

deeper layers ($>$200 m) sheltered from air–sea ice–ocean interactions. Values close to 1 indicate a dominance of heave, and those close to 0 denote that $\Delta\theta$ is dominated by isopycnal property changes.

Both HVE and WMP contributions act in the Amundsen Sea, although their importance depends on the depth and the trough system analyzed (Fig. 3). There are two clear regimes where HVE is more important over a broad area: (i) the upper layers (Fig. 3a), likely due to variability in the mixed layer depth, and (ii) layers deeper than 800 m to the north of the Amundsen Sea continental shelf (Fig. 3d), associated with dynamical variability in the ACC (e.g., Firing et al. 2017). In turn, HVE and WMP are dominant in different regions at intermediate depths of 300–800 m, where the CDW-derived warm waters flood the continental shelf.

WMP contributes more to θ variability within the Dotson–Getz trough, accounting for $>$0.8 of the variance below 300 m (Figs. 3b,c). Its importance decreases toward the Pine Island–Thwaites troughs, where WMP accounts for $<$0.5 of the variance, with lower values at greater
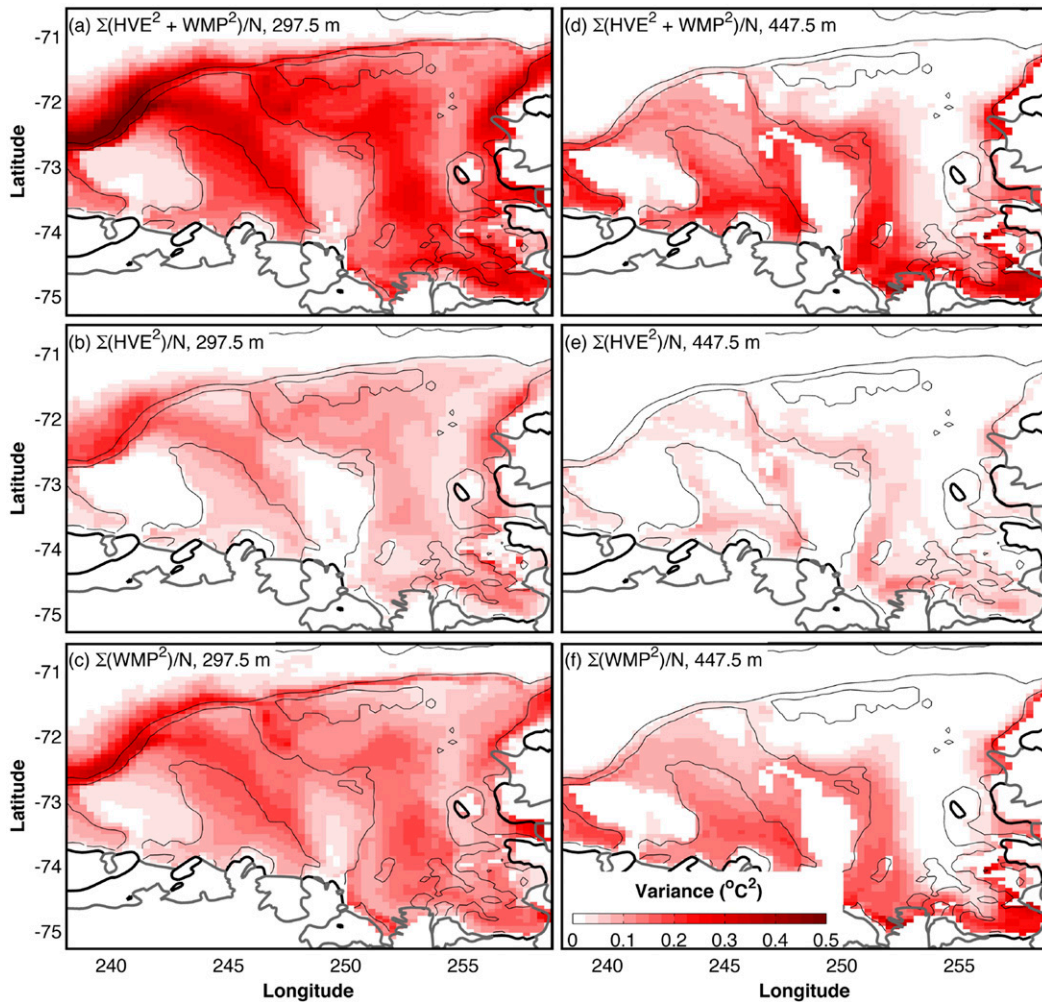
FIG. 4. Variance of the (a),(d) reconstructed $\Delta\theta$, (b),(e) heave (HVE), and (c),(f) water mass property changes (WMP) components near (left) 300- and (right) 450-m depth between 2000 and 2014; $N = 15$ years $\times$ 12 months.

depths (Figs. 3b,c). In the inner Pine Island–Thwaites troughs and its entrances, HVE is the main contributor to the reconstructed $\Delta\theta$ below 400 m, reaching ratios > 0.8 at 520 m and deeper (Figs. 3c,d). Note, however, that $\Delta\theta$ variance is reduced in these regions (Fig. 4d). Temperature variability at depths shallower than 400 m (not shown) and near the ice shelf calving fronts (Figs. 3b,c) is dominated by WMP-related processes. This pattern is likely derived from mixing with glacial meltwater (Jourdain et al. 2017; Naveira Garabato et al. 2017) and highly localized oceanographic processes (St-Laurent et al. 2015; Webber et al. 2017), which may generate complex variations of thermohaline properties. As investigating ice-shelf–ocean interactions is out of scope for this work, we do not consider those coastal processes further.

The spatial patterns in the relative importance of HVE and WMP relate to those of θ variance (Fig. 4).

In general, areas of WMP prevalence are associated with high θ variance. Depths shallower than 300 m are prone to elevated variability in θ, due to proximity to the thermocline (Figs. 4a–c). In the Pine Island–Thwaites troughs, the variance of θ decreases considerably at depths > 400 m, concurrently to a reduction in the significance of WMP relative to HVE (Figs. 4d–f). In this depth range, the vertical distribution of the thermohaline properties is highly homogeneous, except close to the ice shelves (Webber et al. 2017) and along the trough's western flank.

The decomposition in Eq. (2) also reveals that HVE- and WMP-related processes act on different time scales (Figs. 5 and 6). To illustrate this point, we selected five different boxes in the Dotson–Getz trough and Pine Island–Thwaites troughs (Fig. 1a) and evaluated the local temperature variability within each box on different time scales. For each box and
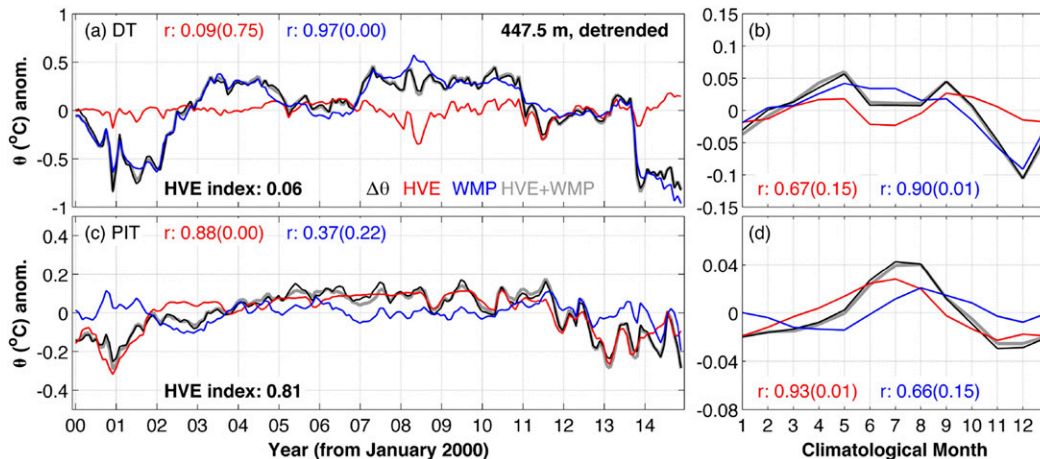
FIG. 5. Monthly time series of $\Delta\theta$ (black), $\Delta\theta$ associated with heave (HVE; red), $\Delta\theta$ associated with water mass property changes (WMP; blue), and the reconstruction (HVE+WMP; gray), all detrended, at 447 m for (a) inner Dotson Trough and (c) inner Pine Island–Thwaites trough (see Fig. 1a). (b),(d) Annual cycle for each region computed as the average for each month of the year of the time series in (a) and (c). January is repeated as the 13th month. Note the different ordinate range in the plots. Correlation coefficients between $\Delta\theta$ and the HVE or WMP terms are shown in colors corresponding to those of the lines. The p values are indicated within parentheses. The HVE index value is shown in bold font in the left panels.

each month, we averaged the detrended temperature at 447.5 m (Fig. 5, left panels; similar results were found for other depths, not shown) and then grouped by month to create a seasonal cycle (Fig. 5, right panels). Within the Dotson–Getz region (Fig. 5a), WMP dominates temperature variability, as previously indicated (Figs. 3c,d). The time series of WMP in the inner Dotson Trough (DT) box follows closely the pattern of $\Delta\theta$ [$r = 0.97$; $r = 0.78$ in the Dotson Shelf Break box (DSB), not shown]. This WMP dominance stems mainly from long periods (>12 months). HVE has a stronger imprint on temperature variability on shorter time scales (<12 months) than on longer periods (>12 months), as seen by the coincidence of peaks and troughs in the time series (Fig. 5a) and in a coherence analysis (Fig. 6a). In the PIT box, HVE has an enhanced importance compared to the Dotson–Getz area. This is reflected in the greater similarity of the HVE term with the $\Delta\theta$ time series (Fig. 5c; $r = 0.88$), and in the higher coherence between the two variables on interannual time scales (>12 months) in the PIT area (Fig. 6b). The annual cycle of θ is dominated by WMP in the DT box (Fig. 5b), and by HVE in the PIT box (Fig. 5d).

The extent to which the two troughs show opposite HVE–WMP partitioning over a range of time scales is striking. While both HVE- and WMP-related processes act to modulate the deep θ variability over the Amundsen Sea continental shelf, their relative importance depends on the trough analyzed and the time scales involved. Next, we will consider the main

driving forces and underpinning mechanisms of each contribution.

b. Dynamical drivers of heave

HVE entails vertical movements of isopycnals, which can lead to warming or cooling. In this section, we assess the association of heave-induced θ variability with changes in Ekman pumping and in the CDW inflow to the continental shelf. While variations in Ekman pumping will affect most of the water column from the top downward, perturbations to the inflow of CDW across the shelf break will modify the volume of the shelf's deeper layers, inflating or deflating the denser classes and generating a vertical displacement of isopycnals.

Variability in Ekman pumping is considered in the eastern Amundsen Sea, where HVE dominates (Fig. 7). We chose an area within the Pine Island–Thwaites troughs and calculated the month-to-month rate of change of the depth of the isopycnal $\gamma^n = 28.00 \text{ kg m}^{-3}$, that is, $\partial z/\partial t$. To circumvent the constraint of the model's limited vertical resolution, γ^n was linearly interpolated in the vertical with a 1-m spacing. The average depth of this isopycnal is approximately 400 m in the eastern Amundsen Sea. The time series of $\partial z/\partial t$ is correlated with that of the local Ekman pumping (Fig. 7a; $r = 0.56$, $p < 0.01$). The correlation decreases to $r = 0.36$ ($p = 0.01$) when the mean annual cycles are removed, suggesting that Ekman pumping is particularly important on seasonal time scales. Composite analysis indicates that the Pine Island–Thwaites troughs generally host anomalous
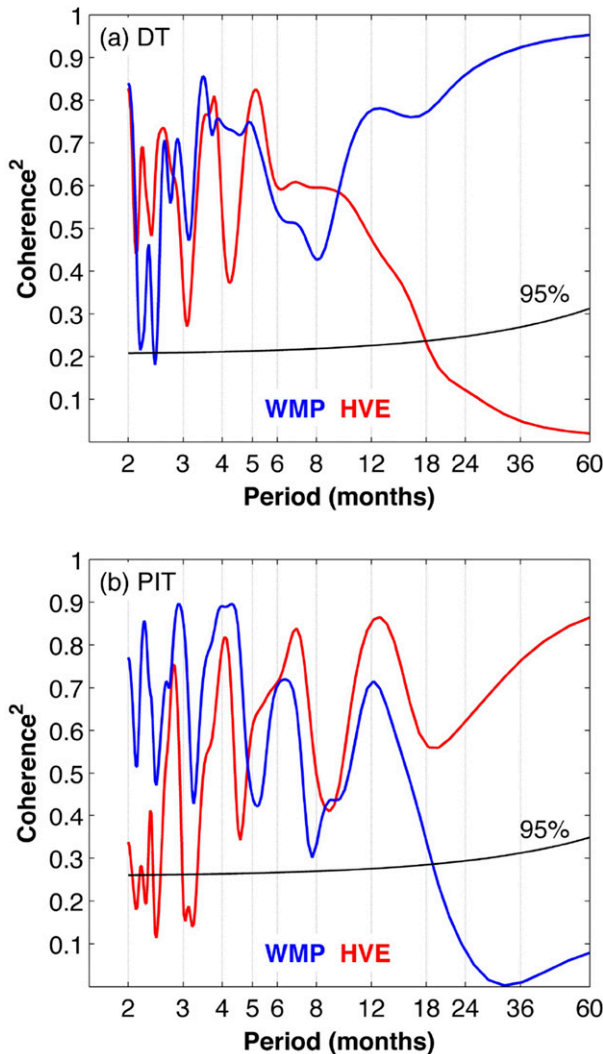
FIG. 6. Coherence between the detrended, reconstructed $\Delta\theta$ and the WMP (blue) and HVE (red) components at 447 m for the regions of (a) Dotson Trough and (b) Pine Island–Thwaites trough. The original time series are presented in Figs. 5a and 5c. Significance bounds (black) are calculated from Eq. (5.173) of Thomson and Emery (2014).

Ekman downwelling (Fig. 7b) when the selected isopycnal deepens in the area. This process expands the cold upper layer, leading to a reduction in the temperature of deeper layers (Fig. 7d). In turn, the troughs are affected by anomalous Ekman upwelling (Fig. 7c) when the selected isopycnal shoals, expanding the warm deeper layers and thus raising the temperature of intermediate and deep levels (Fig. 7e). This association between Ekman pumping and heave-induced temperature variability agrees with recent findings (Kim et al. 2017; Webber et al. 2019). The significant link between Ekman pumping and isopycnal heaving conforms to expectations, and may partly explain the HVE component of θ variability

(Figs. 7d,e). However, the magnitude of $\partial z/\partial t$ substantially exceeds that of the Ekman pumping velocity in many periods (Fig. 7a), suggesting that other mechanisms may contribute notably to displacing isopycnals vertically. The role of changes in lateral advection is considered next.

The CDW inflows crossing the PITE and PITW sections mediate the heat transport toward the inner Pine Island–Thwaites troughs (Nakayama et al. 2013). We investigate the relationship between the HVE contribution to temperature variability in the PIT and the southward deep flow crossing the PITE and PITW sections. The time-averaged CDW inflow through the PITE section conveys 0.12 ± 0.04 Sv (1 Sv $\equiv 1 \times 10^6\,\mathrm{m^3\,s^{-1}}$; Fig. 8a) in the model, in agreement with observations (Azaneu 2019). CDW transport through the PITE section and HVE at PIT are significantly correlated at the 95% confidence level ($r = 0.39$ at zero lag), with maximum correlation when transport leads HVE by 2–4 months ($r = 0.45$; considering the nonfiltered transport). Note, that the correlation is stronger on interannual than on intra-annual time scales (Fig. S10), although a coherence analysis suggests that significant correlation also occurs at 3- and 5-month periods (Fig. S11). The transport is positively correlated to heave-induced θ variability over most of the Pine Island–Thwaites troughs (Fig. 8b). The signal of the positive correlation follows the path of the inflowing CDW southward as far as the Pine Island Ice Shelf. Isopycnal heaving is higher when more CDW flows onto the continental shelf. The spatial map of correlation exhibits negative values near the ice shelf calving fronts. These may indicate that freshwater discharge and mixing with glacial meltwater, linked to circulation cells induced by melting (Jourdain et al. 2017; Kimura et al. 2017; Naveira Garabato et al. 2017), affect the isopycnal depths locally. The maximum correlations (Fig. 8c) between transport and HVE in the trough occur when HVE lags PITE transport, with the lag increasing from 2–4 months in the PIT box to 6–8 months in southern areas away from the shelf break (Fig. 8d), indicating that the signal propagates southward. The 2–4 month lags agree with the characteristic speed of advective propagation in the model, for example, considering the mean poleward speed of $2\,\mathrm{cm\,s^{-1}}$ crossing the PITE section and a distance of ~170 km between the PITE section and PIT box. The propagation speed of warm anomalies is higher than for cold anomalies in the model (Kimura et al. 2017).

The analysis was repeated for the inflow transport through PITW but, despite exhibiting similar spatial structure to Figs. 8b–d, the magnitude of the diagnosed correlations is smaller and less significant
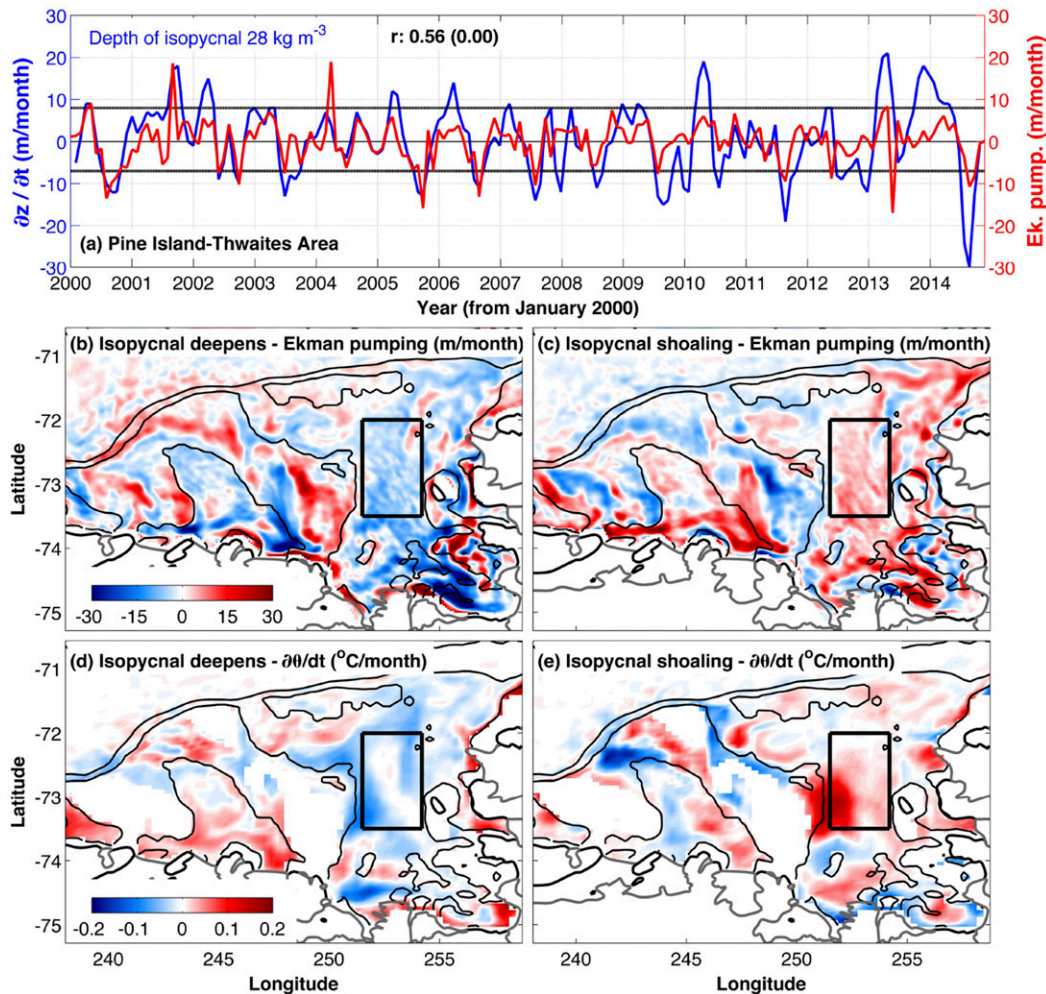
FIG. 7. (a) Detrended rate of change in the depth of the 28.00 kg m^{-3} isopycnal (blue) and local Ekman pumping velocity (red) within the Pine Island–Thwaites Embayment [black squares in (b) and (c)]. Time means were removed. Correlation coefficient and p value are indicated. The 20th and 80th percentiles are depicted (black lines). Composites of Ekman pumping anomaly for the periods (b) below the 20th percentile and (c) above the 80th percentile, based on the vertical shifts of the isopycnal. Composites of the $\partial\theta/\partial t$ anomaly at 447 m for the periods (d) below the 20th percentile and (e) above the 80th percentile.

(not shown). The average time-mean CDW transport through PITW is 0.06 ± 0.02 Sv into the trough, slightly smaller than in observations (Walker et al. 2007; Assmann et al. 2013). Our results thereby suggest that, although the CDW inflows through the PITE and PITW sections contribute to the deep heat content of PIT, the inflow via PITE is more important to the denser CDW classes, as found from observations (Nakayama et al. 2013). We note that in this model, heat transport from PITE is also better correlated with the Pine Island Ice Shelf melting variability (Kimura et al. 2017).

In summary, both changes in local Ekman pumping and in the inflow of CDW through PITE are significant

drivers of heave-induced temperature variability in the Pine Island–Thwaites troughs.

c. Dynamical drivers of isopycnal property changes

Variations in WMP occur by changes in the water mass properties without shifts in the density field. Thus, it is likely that WMP stems from the advection of new water masses onto the Amundsen Sea continental shelf. In this section, we discuss the possible drivers of WMP.

The time series of the WMP contribution to θ variability at 447.5 m in the five Amundsen Sea boxes (Fig. 1a) are compared to the bottom-enhanced southern flow anomaly crossing the corresponding sections
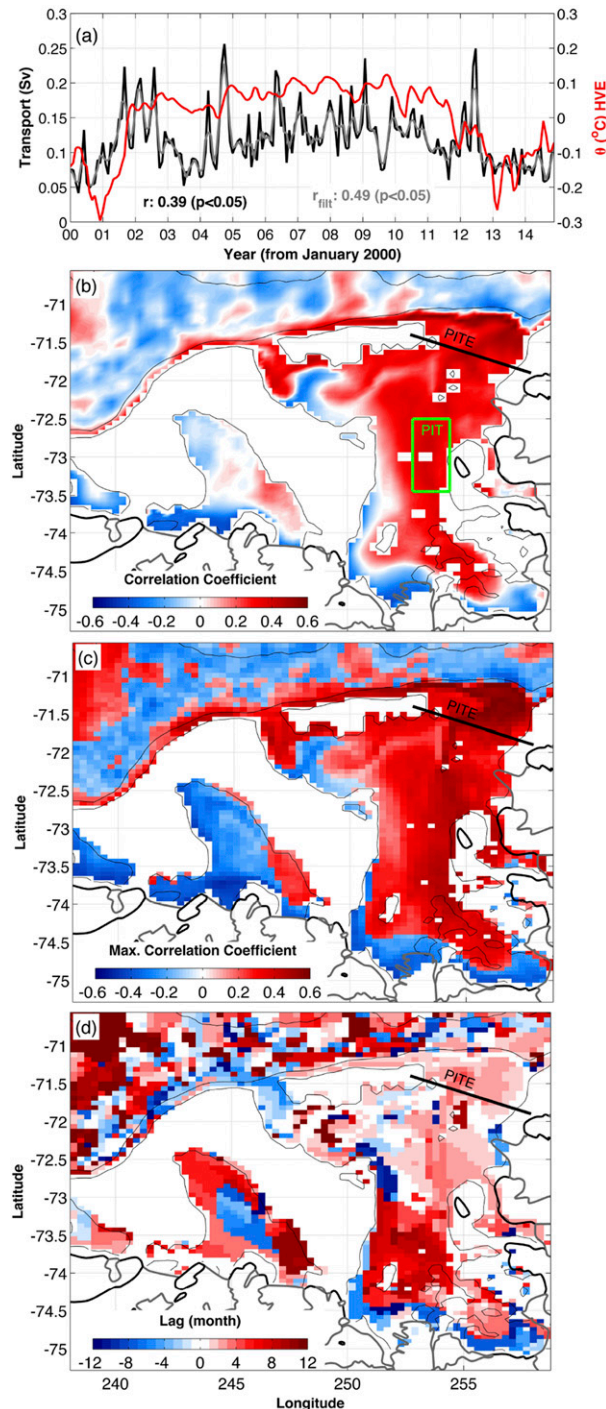
FIG. 8. (a) Poleward transport of waters denser than $\gamma^n >$ 28.00 kg m^{-3} at section PITE (black; 3-month running mean smoothed in gray), and θ variability due to HVE at 447 m within the PIT area (red), outlined in (b). Correlation coefficient and p value are indicated in colors corresponding to those of the lines. Trends and annual cycles were removed. (b) Correlation between the poleward transport at PITE and the temperature variability due to HVE at 447 m in each grid cell. Section PITE (thick black line) and area PIT (green rectangle) are indicated.

upstream of each area (Figs. 1b and 9a). Cross-section velocities are assumed to be representative of the along-slope undercurrent and its southward-deflected branches, which carry warm waters onto the continental shelf (Assmann et al. 2013; Walker et al. 2013). This is evidenced by the spatial coherence of the along-slope flow crossing the ''slope'' section and the bottom speed in the model (where speed $= \sqrt{u^2 + v^2}$), which reproduces the undercurrent pathways and can be used as an indicator of the intensity of the inflow into the Amundsen Sea troughs (Fig. 9a). Figures 9b and 9c shows that the WMP component in each of the Dotson–Getz trough boxes relates closely to the cross-section velocity, that is, WMP-induced θ rises in association with elevated velocity at the shelf break and along the inner trough. These relationships are strongest when the higher-frequency variability of the currents is smoothed by a 3-month running-mean filter. The relationship between WMP and the bottom-enhanced southern flow's intensity weakens toward the eastern Amundsen Sea (Figs. 9d–f), where the WMP contribution is smaller (Fig. 3). Conversely, a significant relationship is observed between the bottom-enhanced southern flow's strength and HVE in the PITE and PIT areas (Figs. 9e,f), in agreement with the notion of expansion (contraction) of the deep layer due to an increased (reduced) volume inflow of CDW (Fig. 8), introduced in section 3b.

The spatiotemporal relationship between the modeled bottom speed and the bottom WMP-induced θ variability is assessed through maximum covariance analysis (MCA; Wallace et al. 1992). The MCA technique extracts the main modes of the cross-covariance matrix between two datasets. Figure 10 shows the first mode of the covariability between bottom speed and bottom WMP anomalies after detrending and deseasonalizing. The mode, which explains 88% of the squared covariance, reveals that an intensified undercurrent is linked to WMP-induced warming of the bottom layers of the Dotson–Getz trough and the coastal areas, and to WMP-induced bottom cooling in the Pine Island–Thwaites troughs (Figs. 10a,b). The cool signal is linked to the inflow of a deeper offshore water type from near the maximum salinity core of CDW, which is slightly colder than the maximum θ core of CDW (not shown). Significant signals are restricted to regions shallower than 1000 m.

←

Isobaths of 500, 1000, and 3000 m are shown (thin black lines). (c) Maximum correlation coefficient from a lagged correlation analysis and (d) corresponding lag of maximum correlation in months.
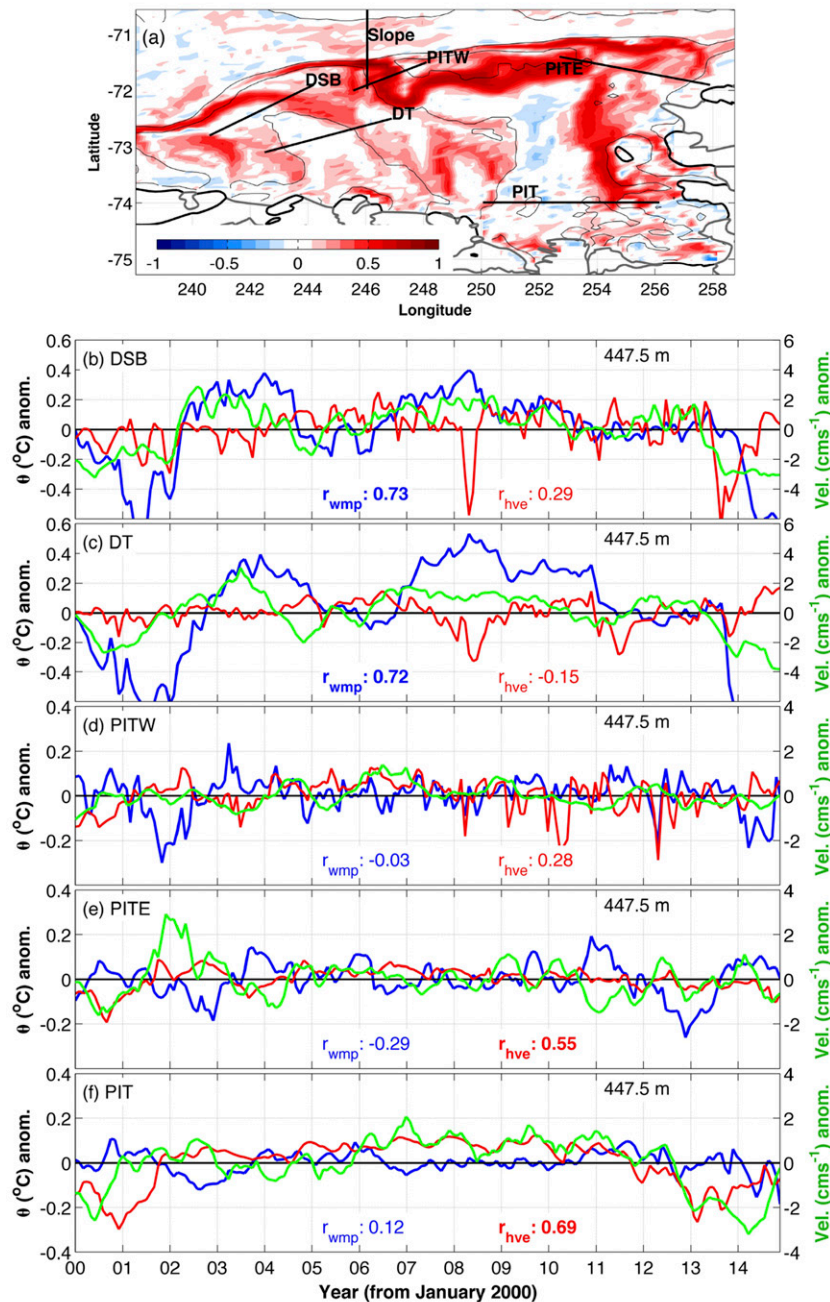
FIG. 9. (a) Map of correlation between the undercurrent velocity crossing the "Slope" sec-
tion and bottom speed. Trends and seasonal cycles were removed. (b)–(f) Time series of
θ anomaly associated with WMP (blue) and HVE (red) in the areas indicated in Fig. 1a and the
bottom enhanced southern flow anomaly (green) crossing the respective section (Fig. 1b).
Undercurrent velocity is smoothed with a 3-month running mean. Trends and seasonal cycles
were previously removed. Correlation coefficients between velocity and θ decomposition terms
are indicated in the colors corresponding to those of the lines. Bold values denote $p < 0.05$.

The expansion coefficients of the MCA are significantly
correlated at the 99% level ($r = 0.77$, explaining most of
the WMP variance; Fig. 10c). The MCA was repeated
for the bottom speed and HVE anomalies (not shown),

and one observes similar structure of an association
between the bottom speed and HVE-induced bottom
warming of the Pine Island–Thwaites troughs, in agree-
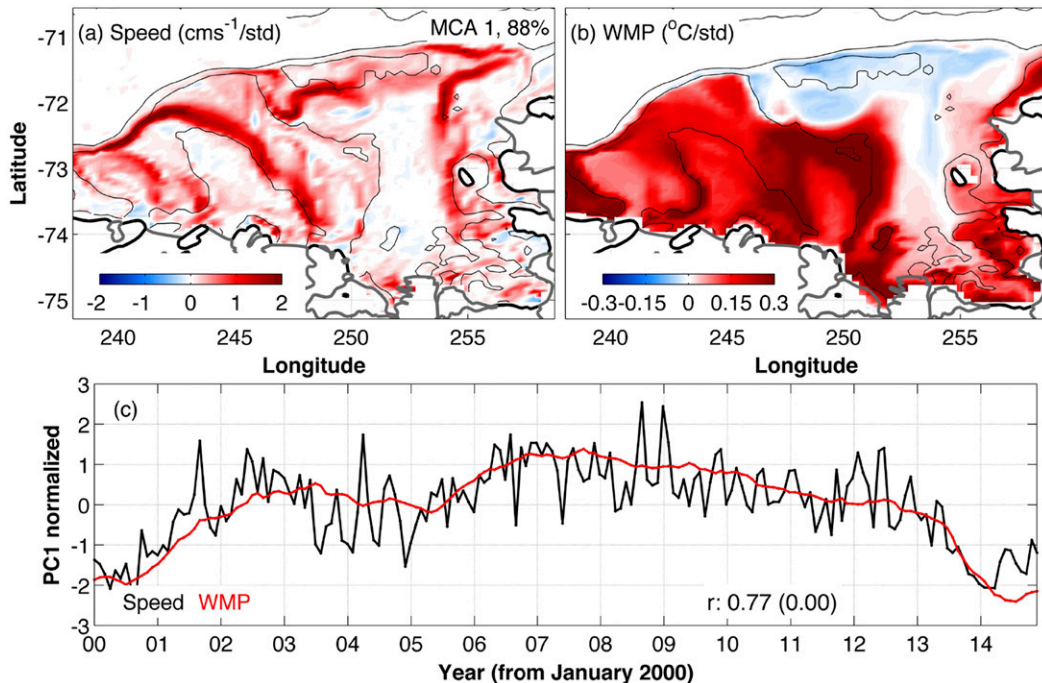ment with Figs. 8 and 9.

FIG. 10. First spatial mode of the maximum covariance analysis of (a) bottom speed anomaly and (b) bottom temperature anomaly associated with WMP. Trends and seasonal cycles were previously removed. Isobaths of 500, 1000, and 3000 m are depicted. (c) Expansion coefficients of speed anomaly (black) and WMP (red). The correlation coefficient and p value (in parentheses) are given.

d. Driving force of undercurrent variability

The undercurrent is a feature that follows the slope and eventually enters the troughs, bringing new warm waters onto the shelf (Fig. 10). It is thought that this feature affects the heat transport toward the Amundsen Sea continental shelf (Assmann et al. 2013; Kimura et al. 2017); however, few observational studies have considered what modulates this current at the continental slope, given the scarcity of in situ data (Walker et al. 2013). Here, we assess the relationship between bottom speed anomaly in the model, which contains clear signatures of the undercurrent and its bottom-enhanced southern flow extension (Fig. 10a), and the zonal ocean surface stress (τ_U) anomaly. The first MCA mode of these two variables explains most (~95%) of their squared covariance, after detrending and deseasonalizing (Fig. 11). The explained covariance changes nontrivially depending on the period of analysis, but the identified spatiotemporal patterns are insensitive to that choice (not shown). The spatial representation of the first mode indicates that the bottom speed along the slope (Fig. 11a) is intensified in association with an anomalous eastward τ_U, equivalent to stronger offshore eastward winds and weaker westward winds on the continental shelf (Fig. 11b). The bottom speed signal extends along the eastern flank of

the Dotson–Getz trough and across the entrances of PITW and PITE. The expansion coefficients of τ_U and bottom speed are significantly correlated ($r = 0.65$) at the 99% confidence level (Fig. 11c). Similar results were found with the zonal wind stress anomaly in lieu of τ_U, suggesting that the role of sea ice in modifying the momentum transfer from the wind is not essential in determining the variability of bottom flows (not shown), as it is for the local Ekman pumping (Fig. 2).

4. Discussion

We have shown that the two components of deep temperature variability in the Amundsen Sea continental shelf, HVE and WMP, dominate in different subregions and are driven by distinct mechanisms. Vertical displacements of isopycnals in the PIT area are forced by Ekman pumping and by modulation of the volume of CDW entering through PITE. In turn, the strength of the flow in the Dotson–Getz trough is responsible for bringing new varieties of CDW onto the area, and thus controls local WMP variability.

WMP is generally associated with elevated temperature variance (Fig. 4). To illuminate the reasons for this, we display the differences in θ, velocity, and depth of the shallow isopycnal $\gamma^n = 27.95$ kg m^{-3} (with a typical
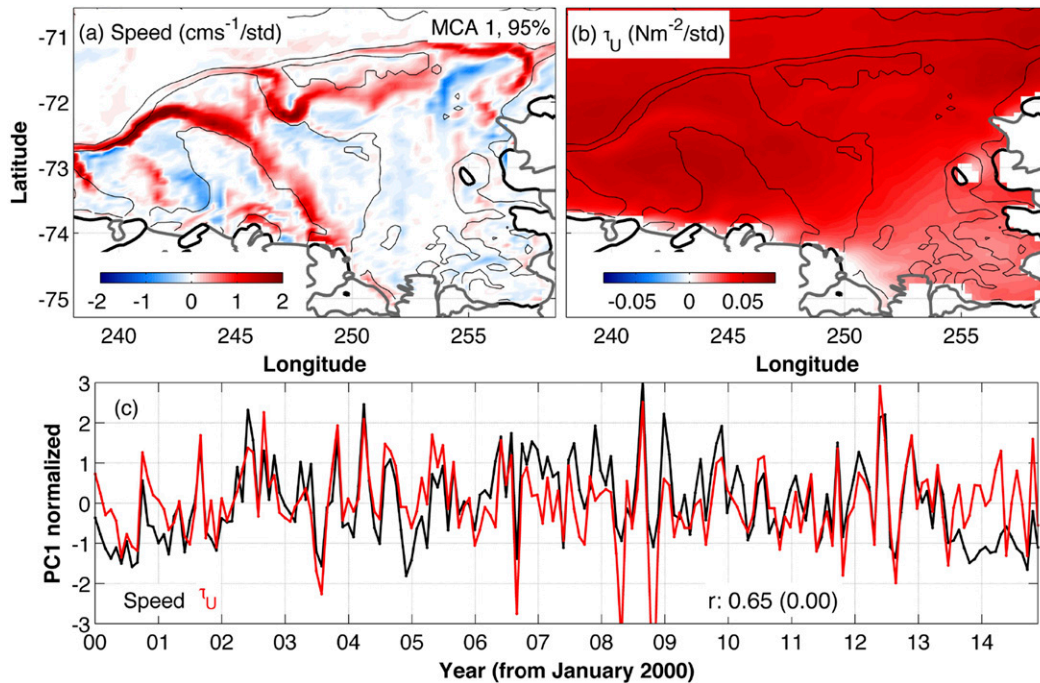
FIG. 11. First spatial mode of the maximum covariance analysis of (a) bottom speed anomaly and (b) zonal ocean surface stress (τ_U). Trends and seasonal cycles were previously removed. Isobaths of 500, 1000, and 3000 m are depicted. (c) Expansion coefficients of speed anomaly (black) and τ_U (red). The correlation coefficient and p value (in parentheses) are given.

depth of ~320 m in the eastern Amundsen Sea, deepening near the ice shelves; Fig. S12) between periods of stronger and weaker undercurrent crossing the Pine Island section (Fig. 12). During stronger undercurrent periods, a greater volume of CDW inflows the PIT at levels denser than $27.95\,\mathrm{kg\,m^{-3}}$, particularly via PITE, and induces a shoaling of isopycnals along the eastern flank of the PIT (Fig. 12b). The increased volume of the layers denser than $27.95\,\mathrm{kg\,m^{-3}}$ enhances zonal isopycnal slopes, leading to an intensification of the southward flow (relative to the surface) along those isopycnals through geostrophy (Figs. 12b,c). The strengthened inflow brings warm waters from the shelf break further into the PIT, raising the temperature on those isopycnals along the inflow's path. The inflow of warmer waters likely induces a displacement of ambient waters farther south into the trough, leading to widespread warming on the $27.95\,\mathrm{kg\,m^{-3}}$ isopycnal.

The wind has been described as an important agent in modulating the volume of the CDW-derived waters inflowing the Amundsen Sea continental shelf (Thoma et al. 2008; Steig et al. 2012; Wåhlin et al. 2013; Dutrieux et al. 2014; Webber et al. 2019). Further, it has been suggested that variations in the velocity of the deep currents control the heat transport toward the continental shelf (Assmann et al. 2013; Kalén et al. 2016;

Kimura et al. 2017). Consistent with these previous works, we have presented evidence indicating that τ_U primarily regulates the intensity of the along-slope undercurrent (Figs. 11a,b), which in turn impacts θ variability in the eastern (Fig. 8a) and western (Fig. 10b) Amundsen Sea through distinct mechanisms: WMP-based in the Dotson–Getz trough, and HVE-based in the Pine Island–Thwaites troughs (Fig. 3). Ultimately, a stronger (weaker) undercurrent leads to warming (cooling) in both trough systems.

Given this dichotomy of processes, why is the response to an acceleration (or deceleration) of the undercurrent the same for all troughs? To elucidate the answer, Fig. 13 shows composites of the hydrographic properties across the shelf break for periods of intensified undercurrent crossing the sections along the Dotson–Getz and Pine Island–Thwaites troughs (Fig. 1b). The response to a weaker undercurrent is qualitatively opposite to that illustrated here (not shown). As the undercurrent accelerates, anomalous upwelling occurs above the continental slope, leading to uplifting of the deeper isopycnals (see, e.g., $\gamma^n = 28.00\,\mathrm{kg\,m^{-3}}$; Figs. 13b and 13f). This brings warmer waters onto the shelf, and both troughs are consequently warmed mostly at depth (Figs. 13c,g). The uplifting of isopycnals above the continental slope in response to an intensification of the undercurrent is broadly consistent with expectations
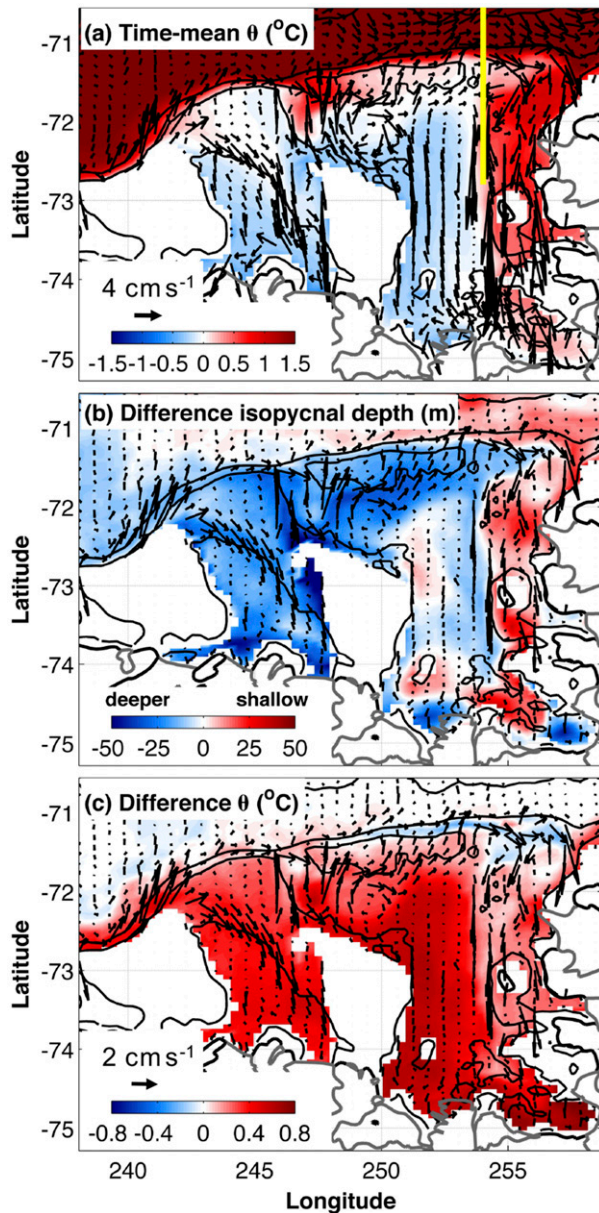
FIG. 12. (a) Time-mean θ and velocity (vectors plotted every two grid cells) along isopycnal $\gamma^n = 27.95 \, \text{kg m}^{-3}$. The yellow line depicts the Pine Island section. (b) Difference of the isopycnal depth and velocity between the composites of intensified and reduced undercurrent periods (defined across Pine Island section; see Fig. 13a for the selected periods). (c) As in (b), but for difference of θ. Isobaths of 500, 1000, and 3000 m are shown by black lines. Large white areas are regions where $\gamma^n < 27.95 \, \text{kg m}^{-3}$.

from bottom Ekman dynamics (Garrett et al. 1993; Rossi et al. 2010; Wåhlin et al. 2012), whereby an increase in near-bottom flow speed of $O(0.05–0.1) \, \text{m s}^{-1}$ is predicted (see Garrett et al. 1993) to induce a vertical displacement of $O(10–100)$ m for the region's ambient planetary vorticity ($\sim-1.4 \times 10^{-4} \, \text{s}^{-1}$), buoyancy

frequency ($\sim1.2 \times 10^{-3} \, \text{s}^{-1}$), and topographic slope (0.03–0.06), in line with the model's diagnostics (Fig. 13). It is likely, however, that the model's vertical resolution is suboptimal to represent the flow–topography interaction mechanism governing the isopycnals' adjustment (e.g., Ruan et al. 2017). Unraveling these dynamics will be the focus of future work.

The distinct mechanisms underpinning θ variability in the two trough systems of the Amundsen Sea are related to differences in the configuration of the density field above the continental slope and in the shelf break depth. The thermocline (characterized here by the 0°C isotherm) shoals eastward across the Amundsen Sea (Fig. 14), whereas the shelf break is shallower in the western (~450 m) than in the eastern (~500 m) Amundsen Sea (Fig. 13). As a result, access of CDW to the Dotson–Getz trough is partially restricted by topography, but is essentially unimpeded in the Pine Island–Thwaites troughs (e.g., see depth of $\gamma^n = 28.00 \, \text{kg m}^{-3}$; Figs. 13c and 13g). CDW may then flood the eastern Amundsen Sea continental shelf continuously (Jacobs et al. 2012), such that the deep thermohaline characteristics inside the Pine Island–Thwaites troughs experience little variability (Fig. 4d) and are modified primarily via heaving of the ambient hydrographic structure (Figs. 3b,c). This heave is regulated by Ekman pumping (Fig. 7) and changes in the CDW inflow to the trough via PITE (Fig. 8a), which are themselves coupled to the vertical displacement of isopycnals at the shelf break. In contrast, in the Dotson–Getz trough, substantial CDW access primarily occurs at times when the undercurrent is strong. In these instances, a largely unmodified variety of CDW floods the trough and generates a WMP signal (Fig. 13e). HVE also affects the deep temperature at some locations (e.g., at the shelf break and close to the coast) following perturbations in Ekman pumping (not shown), but its effect is modest (Figs. 5a and 13d).

Previous observations and modeling suggested that the temperature variability in the Amundsen Sea troughs responds to Ekman pumping at the shelf break (Kim et al. 2017; Webber et al. 2019). However, this forcing mechanism alone cannot fully explain the θ variability associated with HVE in all troughs in our simulation (Fig. 7a). The results of Kim et al. (2017), in particular, appear at odds with our finding that WMP underpins the bulk of temperature variability in the Dotson–Getz trough. This apparent contradiction may be resolved by noting that in the period analyzed by those authors (2011–12), HVE dominated θ changes in most of that trough (Fig. 5a; not shown for other locations). An analysis of mooring measurements in the
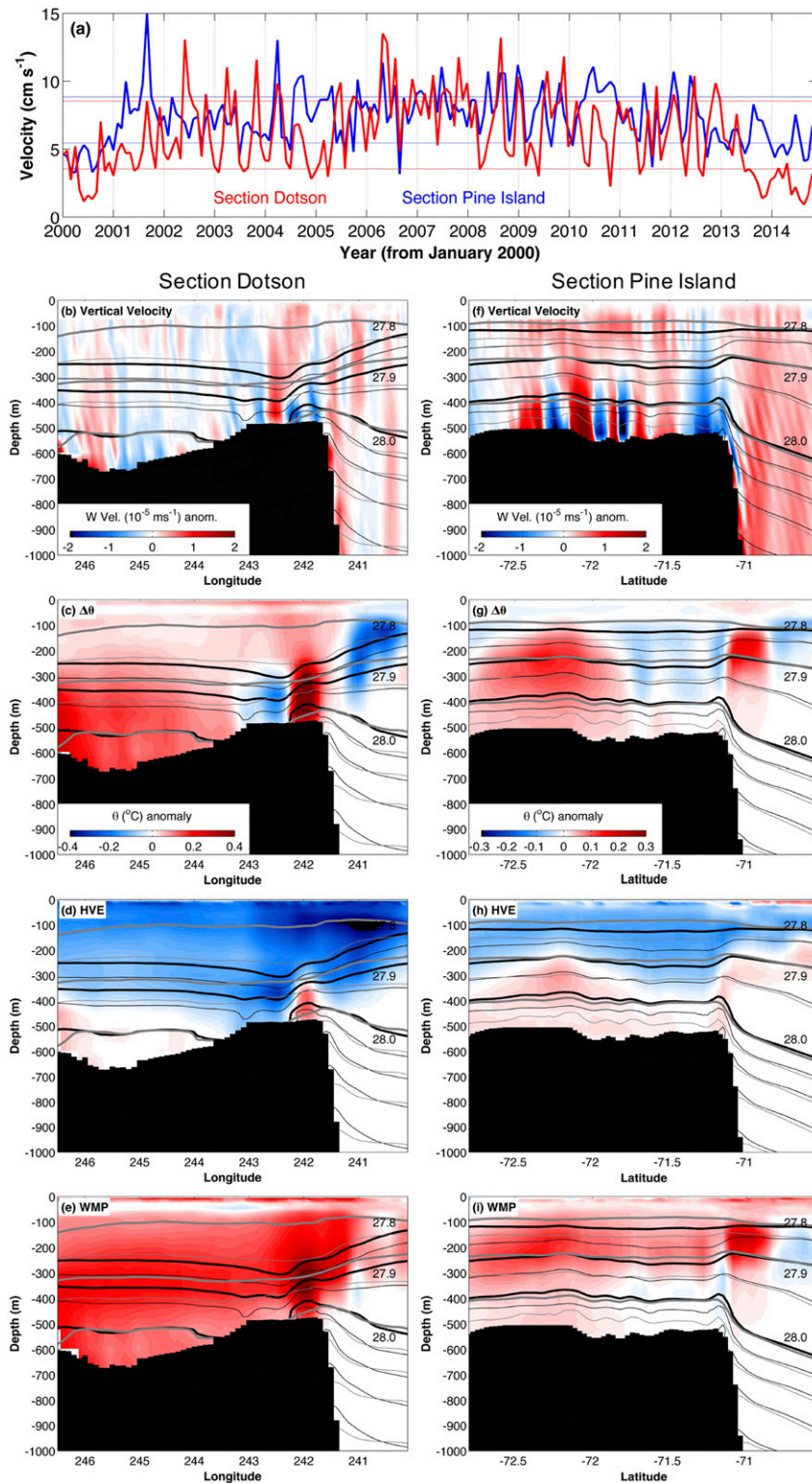
FIG. 13. (a) Time series of maximum cross-section velocity through the Dotson (red) and Pine Island (blue; Fig. 1b) sections. The 20th and 80th percentiles are shown by the solid horizontal lines according to the corresponding colors. Trends and seasonal cycles were previously removed. Composites for the intensified undercurrent periods (i.e., 80th percentile)

Dotson–Getz trough (Wåhlin et al. 2013) supports our findings, and shows that (i) the model's decomposition of θ variability is realistic, and (ii) HVE dominates on short time scales between 2010 and 2013 (Fig. S13). Thus, Ekman pumping may be a prevalent player in specific short periods in the Dotson–Getz trough. Yet on longer time scales, WMP-related processes govern the delivery of CDW across the western Amundsen Sea (Fig. 3).

Our results are in agreement with the recent work of Webber et al. (2019), who showed that the increased inflow of CDW and thermocline shoaling occurring in the eastern Amundsen Sea in warmer years are related to wind forcing and a stronger circulation in the area. Those authors point to Ekman suction at the continental slope as the key driver of CDW inflow onto the shelf on interannual to decadal time scales. In contrast, our model stresses the significance of wind-driven intensification of the undercurrent at the shelf break, which enhances the local heat content via increased volume transport of CDW into the trough and via Ekman pumping on the continental shelf shifting the depth of the isopycnals (both of which affect the HVE component of θ variability). Thus, our mechanistic interpretation of how warming of the eastern Amundsen Sea occurs is partially at odds with that of Webber et al. (2019). Further, our work expands those authors' picture by showing that the western and eastern Amundsen Sea exhibit different mechanisms controlling variations in the CDW delivery to the continental shelf. We note, however, that the simulation period, temporal resolution and atmospheric forcing of the model of Webber et al. (2019) are different to ours. (Specifically, their model is forced with CFSR atmospheric fields, runs from 1979 to 2011 following a 10-yr spinup with perpetual 1979 conditions, and provides 5-day outputs; whereas our model is forced with ERA-Interim, runs from 1991–2014 without a previous spinup, and provides monthly outputs.)

A narrow eastward undercurrent has been documented in several areas around Antarctica, at the shelf break and continental slope, by closely spaced hydrographic measurements and high-resolution models (Heywood et al. 1998; Smedsrud et al. 2006; Nuñez-Riboni and Fahrbach 2009; Chavanne et al. 2010; Silvano et al. 2019). Based on

our results and previous works (e.g., Walker et al. 2013; Kimura et al. 2017; Webber et al. 2019), it may be concluded that this undercurrent feature is an important element of the oceanic heat delivery toward the ice shelves. However, the undercurrent's formation process remains unclear, with some studies suggesting an association with topographic trapped waves (Middleton and Cirano 1999; Chavanne et al. 2010) and others with thermal wind shear linked to the Antarctic Slope Current (Heywood et al. 1998; Jenkins et al. 2016). Understanding the formation and development of undercurrent systems around Antarctica stands out as an important target for future investigations.

Melting of the ice shelves at the Amundsen Sea's southern rim is primarily regulated by changes in the thermocline depth in front of the ice shelves and in the heat content on the continental shelf farther offshore (Dutrieux et al. 2014; Webber et al. 2017; Davis et al. 2018). Thus, our identification of the processes by which CDW accesses the Amundsen Sea troughs is an important step in understanding the preconditioning, that is, the heat source, for ice shelf melting downstream. While local modulation of the thermocline depth near the ice shelves by wind forcing and/or other localized processes will impact melting most readily, the effectiveness of these local drivers depends on how much warm water is available across the continental shelf.

A synthesis of our main findings is provided in Fig. 15. Eastward τ_U anomalies in the Amundsen Sea are associated with intensification of the undercurrent along the slope, inducing an uplift of isopycnals near the shelf break. At the mouth of the Dotson–Getz trough, the thermocline is roughly at the sill depth, so uplifting of isopycnals results in the inflow of a new, warmer type of CDW into the trough. This explains the primary underpinning by WMP of temperature variability within that trough. In the eastern Amundsen Sea, the thermocline is always shallower than the sill depth, such that uplifting of isopycnals has little effect on what type of CDW flows into the troughs there. Instead, the intensified undercurrent and uplifted isopycnals bring an increase in the volume of CDW entering the trough system, mainly via PITE. Wind forcing in the eastern Amundsen Sea is structured in such a way that Ekman

$\leftarrow$

across the (left) Dotson and (right) Pine Island sections showing (b),(f) vertical velocity anomaly, (c),(g) $\Delta\theta$, (d),(h) HVE component, and (e),(i) WMP component. The 27.8, 27.9, and 28.0 kg m^{-3} isopycnals are shown by thick lines. Isopycnals between these values are spaced every 0.05 kg m^{-3}, and every 0.02 kg m^{-3} for $\gamma^n > 28.0$ kg m^{-3}. Black (gray) contours refer to the intensified (reduced) undercurrent periods.
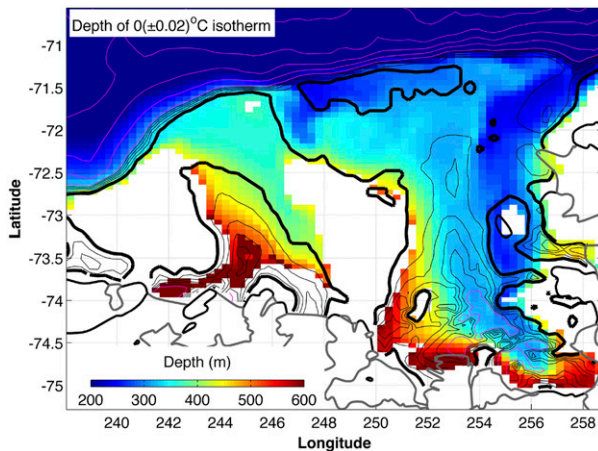
FIG. 14. The 2000–14 time-mean depth of the 0°C isotherm. The 500-m isobath is indicated by the thick black line. A white mask is used when the 0°C isotherm is not present, or if it is shallower than 100 m. The 1000–3000-m isobaths are shown in magenta every 500 m. The 600–900-m isobaths are shown as thin black lines every 100 m. The colorbar is saturated to highlight the depth difference between Dotson and Pine Island Embayment.

pumping also plays a role. Both mechanisms, that is, stronger inflow and increased Ekman upwelling, lead to HVE-based warming of the deeper layers within those troughs. Closer to the ice shelves, freshwater discharge may modify this picture.

In the present work, we analyzed the local forcings and processes governing temperature variability on the Amundsen Sea continental shelf. However, one must keep in mind that remote drivers might also affect the region's heat content via changes in the pathways or properties of offshore water masses (Nakayama et al. 2018), and/or the remote wind-forced generation and propagation of barotropic Kelvin waves around Antarctica (Kusahara and Ohshima 2014; Spence et al. 2017; Webb et al. 2019). While our results are most relevant for temperature changes in the Amundsen Sea on time scales of months to years, remote forcings are likely to exert an increasingly important influence on temperature variability on longer time scales (Spence et al. 2014; Nakayama et al. 2018), which may affect the ice shelves' configuration over periods of decades to centuries (Jenkins et al. 2018).

Finally, we acknowledge several caveats of our study. The relatively coarse temporal resolution of the model output impeded assessment of the fast response of water masses in the troughs to winds or other forcings (e.g., Wåhlin et al. 2012, 2013; Davis et al. 2018). Further, although the model's spatial resolution is sufficient to reproduce CDW inflows onto the continental shelf (Nakayama et al. 2014), it may not capture all the important processes implicated in the interaction of the flow with topography (e.g., St-Laurent et al. 2013), as
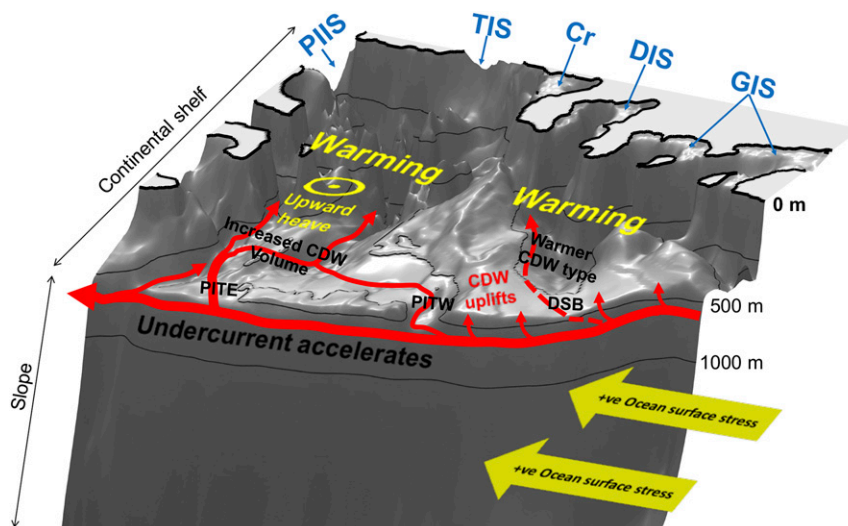

FIG. 15. Schematic view of the processes underpinning a period of warming in the Amundsen Sea. Zonal ocean surface stress accelerates the undercurrent, which uplifts isopycnals above the slope and enhances the inflow of CDW onto the continental shelf. A shallower (deeper) shelf break (thermocline) in the Dotson Trough leads to the inflow of a new, warmer type of CDW, resulting in a dominance of WMP-related warming in that trough. In the Pine Island Embayment, the deeper (shallower) shelf break (thermocline) enables continuous access of CDW to that trough system. A higher volume of CDW entering those troughs displaces vertically the on-shelf isopycnals, leading to a prevalence of HVE-related warming in that area.

well as mesoscale eddy- and tide-induced transports (Thompson et al. 2014; Stewart et al. 2018). Nevertheless, the favorable comparison between observations and modeling results (Figs. S2–S7) and the sound response of the model's dynamics to wind forcing (Fig. S8) give confidence in our main conclusions.

5. Conclusions

A variety of processes have been suggested to regulate the inflow of CDW onto the Amundsen Sea continental shelf, involving wind forcing (Thoma et al. 2008; Kim et al. 2017; Webber et al. 2019), ocean currents (Walker et al. 2013; Assmann et al. 2013; Kimura et al. 2017), and flow–topography interactions (Wåhlin et al. 2012). Here, we showed that many of the processes highlighted in past investigations occur concurrently; however, their relative importance depends on the region and time scales considered. Temperature variability in the western Amundsen Sea is governed primarily by property changes along isopycnals; in contrast, the eastern Amundsen Sea is mainly regulated by changes in temperature due to heaving of isopycnals. Both processes are controlled by wind-forced modulation of the intensity of an along-slope undercurrent. In the western Amundsen Sea, the offshore thermocline lies approximately at the depth of the shelf break, so undercurrent intensification leads to the inflow of a warmer variety of CDW due to uplifted isopycnals at the continental slope. In the eastern sector, the shallower offshore thermocline and deeper shelf break allows CDW to readily access the continental shelf. The volume of CDW entering the trough via the undercurrent, as well as by Ekman pumping within the trough, shape the heaving of isopycnals in that area. Our study is based on ocean modeling, but since the regional dynamics are respected, these results are likely to be relevant to the real ocean. At any rate, it is important that in situ measurements are continued in order to confirm our findings and gain insights pertinent to longer periods.

We conclude that the western and eastern sectors of the Amundsen Sea host different oceanographic regimes, in which the wind controls the oceanic heat delivery to the Antarctic margins via distinct dynamics. This suggests divergent sensitivities to wind forcing in the two areas, and raises the possibility of occurrence of major regime shifts (via, for instance, changes in the depth of the offshore thermocline relative to the shelf break depth; e.g., Jenkins et al. 2016). Our results stress that in order to represent the system realistically, and capture the ocean forcing of ice shelf evolution, climate-scale ocean models need to adequately represent the coupled air–ice–ocean stresses and the undercurrent

dynamics, as well as the processes setting the time-mean geometry of the regional thermocline.

REFERENCES

Antonov, J. I., and Coauthors, 2010: *Salinity*. Vol. 2, *World Ocean Atlas 2009*, NOAA Atlas NESDIS 69, 184 pp.

Assmann, K. M., A. Jenkins, D. R. Shoosmith, D. P. Walker, S. S. Jacobs, and K. W. Nicholls, 2013: Variability of Circumpolar Deep Water transport onto the Amundsen Sea continental shelf through a shelf break trough. *J. Geophys. Res. Oceans*, **118**, 6603–6620, https://doi.org/10.1002/2013JC008871.

Azaneu, M., 2019: Slope exchange processes in the Weddell and Amundsen Seas. Ph.D. thesis, University of East Anglia, 155 pp.

Bindoff, N. L., and T. J. McDougall, 1994: Diagnosing climate change and ocean ventilation using hydrographic data. *J. Phys. Oceanogr.*, **24**, 1137–1152, https://doi.org/10.1175/1520-0485(1994)024<1137:DCCAOV>2.0.CO;2.

Chavanne, C. P., K. J. Heywood, K. W. Nicholls, and I. Fer, 2010: Observations of the Antarctic Slope Undercurrent in the southeastern Weddell Sea. *Geophys. Res. Lett.*, **37**, L13601, https://doi.org/10.1029/2010GL043603.

Christianson, K., and Coauthors, 2016: Sensitivity of Pine Island Glacier to observed ocean forcing. *Geophys. Res. Lett.*, **43**, 10 817–10 825, https://doi.org/10.1002/2016GL070500.

Davis, P. E. D., and Coauthors, 2018: Variability in basal melting beneath Pine Island Ice Shelf on weekly to monthly time-scales. *J. Geophys. Res. Oceans*, **123**, 8655–8669, https://doi.org/10.1029/2018JC014464.

Dee, D. P., and Coauthors, 2011: The ERA-Interim reanalysis: Configuration and performance of the data assimilation system. *Quart. J. Roy. Meteor. Soc.*, **137**, 553–597, https://doi.org/10.1002/qj.828.

Desbruyères, D. G., E. L. McDonagh, B. A. King, and V. Thierry, 2017: Global and full-depth ocean temperature trends during the early twenty-first century from Argo and repeat hydrography. *J. Climate*, **30**, 1985–1997, https://doi.org/10.1175/JCLI-D-16-0396.1.

Dewey, S., J. Morison, R. Kwok, S. Dickinson, D. Morison, and R. Andersen, 2018: Arctic ice-ocean coupling and gyre equilibration observed with remote sensing. *Geophys. Res. Lett.*, **45**, 1499–1508, https://doi.org/10.1002/2017GL076229.

Dutrieux, P., and Coauthors, 2014: Strong sensitivity of Pine Island ice-shelf melting to climatic variability. *Science*, **343**, 174–178, https://doi.org/10.1126/science.1244341.

Firing, Y. L., E. L. McDonagh, B. A. King, and D. G. Desbruyères, 2017: Deep temperature variability in Drake Passage. *J. Geophys. Res. Oceans*, **122**, 713–725, https://doi.org/10.1002/2016JC012452.

Garrett, C., P. MacCready, and P. Rhines, 1993: Boundary mixing and arrested Ekman layers: Rotating stratified flow near a sloping boundary. *Annu. Rev. Fluid Mech.*, **25**, 291–323, https://doi.org/10.1146/annurev.fl.25.010193.001451.

Gourmelen, N., and Coauthors, 2017: Channelized melting drives thinning under a rapidly melting Antarctic ice shelf. *Geophys. Res. Lett.*, **44**, 9796–9804, https://doi.org/10.1002/2017GL074929.

Ha, H. K., and Coauthors, 2014: Circulation and modification of warm deep water on the Central Amundsen Shelf. *J. Phys. Oceanogr.*, **44**, 1493–1501, https://doi.org/10.1175/JPO-D-13-0240.1.

Heywood, K., R. Locarnini, R. Frew, P. Dennis, and B. King, 1998: Transport and water masses of the Antarctic Slope Front system in the eastern Weddell Sea. *Ocean, Ice, and Atmosphere: Interactions at the Antarctic Continental Margin*, S. S. Jacobs and R. F. Weiss, Eds., Antarctic Research Series, Vol. 75, Amer. Geophys. Union, 203–214.

Holland, P. R., N. Bruneau, C. Enright, M. Losch, N. T. Kurtz, and R. Kwok, 2014: Modeled trends in Antarctic Sea ice thickness. *J. Climate*, **27**, 3784–3801, https://doi.org/10.1175/JCLI-D-13-00301.1.

Jacobs, S., A. Jenkins, C. Giulivi, and P. Dutrieux, 2011: Stronger ocean circulation and increased melting under Pine Island Glacier ice shelf. *Nat. Geosci.*, **4**, 519–523, https://doi.org/10.1038/ngeo1188.

——, ——, H. Hellmer, C. Giulivi, F. Nitsche, B. Huber, and R. Guerrero, 2012: The Amundsen Sea and the Antarctic ice sheet. *Oceanography*, **25** (3), 154–163, https://doi.org/10.5670/oceanog.2012.90.

Jenkins, A., P. Dutrieux, S. Jacobs, E. J. Steig, G. H. Gudmundsson, J. Smith, and K. J. Heywood, 2016: Decadal ocean forcing and Antarctic ice sheet response: Lessons from the Amundsen Sea. *Oceanography*, **29** (4), 106–117, https://doi.org/10.5670/oceanog.2016.103.

——, D. Shoosmith, P. Dutrieux, S. Jacobs, T. W. Kim, S. H. Lee, H. K. Ha, and S. Stammerjohn, 2018: West Antarctic Ice Sheet retreat in the Amundsen Sea driven by decadal oceanic variability. *Nat. Geosci.*, **11**, 733–738, https://doi.org/10.1038/s41561-018-0207-4.

Jourdain, N. C., P. Mathiot, N. Merino, G. Durand, J. Le Sommer, P. Spence, P. Dutrieux, and G. Madec, 2017: Ocean circulation and sea-ice thinning induced by melting ice shelves in the Amundsen Sea. *J. Geophys. Res. Oceans*, **122**, 2550–2573, https://doi.org/10.1002/2016JC012509.

Kalén, O., K. M. Assmann, A. K. Wåhlin, H. K. Ha, T. W. Kim, and S. H. Lee, 2016: Is the oceanic heat flux on the central Amundsen Sea shelf caused by barotropic or baroclinic currents? *Deep-Sea Res. II*, **123**, 7–15, https://doi.org/10.1016/j.dsr2.2015.07.014.

Kim, T. W., H. K. Ha, A. K. Wåhlin, S. H. Lee, C. S. Kim, J. H. Lee, and Y. K. Cho, 2017: Is Ekman pumping responsible for the seasonal variation of warm circumpolar deep water in the Amundsen Sea? *Cont. Shelf Res.*, **132**, 38–48, https://doi.org/10.1016/j.csr.2016.09.005.

Kimura, S., and Coauthors, 2017: Oceanographic controls on the variability of ice-shelf basal melting and circulation of glacial meltwater in the Amundsen Sea Embayment, Antarctica. *J. Geophys. Res. Oceans*, **122**, 10 131–10 155, https://doi.org/10.1002/2017JC012926.

Klinck, J. M., 1996: Circulation near submarine canyons: A modeling study. *J. Geophys. Res.*, **101**, 1211–1223, https://doi.org/10.1029/95JC02901.

Kusahara, K., and K. I. Ohshima, 2014: Kelvin waves around Antarctica. *J. Phys. Oceanogr.*, **44**, 2909–2920, https://doi.org/10.1175/JPO-D-14-0051.1.

Large, W. G., J. C. McWilliams, and S. Doney, 1994: Oceanic vertical mixing: A review and a model with a nonlocal boundary layer parameterization. *Rev. Geophys.*, **32**, 363–403, https://doi.org/10.1029/94RG01872.

Locarnini, R. A., A. V. Mishonov, J. I. Antonov, T. P. Boyer, H. E. Garcia, O. K. Baranova, M. M. Zweng, and D. R. Johnson, 2010: *Temperature*. Vol. 1, *World Ocean Atlas 2009*, NOAA Atlas NESDIS 68, 184 pp.

Losch, M., 2008: Modeling ice shelf cavities in a z coordinate ocean general circulation model. *J. Geophys. Res.*, **113**, C08043, https://doi.org/10.1029/2007JC004368.

——, D. Menemenlis, J.-M. Campin, P. Heimbach, and C. Hill, 2010: On the formulation of sea-ice models. Part 1: Effects of different solver implementations and parameterizations. *Ocean Modell.*, **33**, 129–144, https://doi.org/10.1016/j.ocemod.2009.12.008.

Mallett, H. K. W., L. Boehme, M. Fedak, K. J. Heywood, D. P. Stevens, and F. Roquet, 2018: Variation in the distribution and properties of circumpolar deep water in the eastern Amundsen Sea, on seasonal timescales, using seal-borne tags. *Geophys. Res. Lett.*, **45**, 4982–4990, https://doi.org/10.1029/2018GL077430.

Marshall, J., A. Adcroft, C. Hill, L. Perelman, and C. Heisey, 1997: A finite-volume, incompressible Navier-Stokes model for studies of the ocean on parallel computers. *J. Geophys. Res.*, **102**, 5753–5766, https://doi.org/10.1029/96JC02775.

Martinson, D. G., and D. C. McKee, 2012: Transport of warm upper circumpolar deep water onto the Western Antarctic Peninsula continental shelf. *Ocean Sci.*, **8**, 433–442, https://doi.org/10.5194/os-8-433-2012.

Meneghello, G., J. Marshall, M. Timmermans, and J. Scott, 2018: Observations of seasonal upwelling and downwelling in the Beaufort Sea mediated by sea ice. *J. Phys. Oceanogr.*, **48**, 795–805, https://doi.org/10.1175/JPO-D-17-0188.1.

Middleton, J. F., and M. Cirano, 1999: Wind-forced downwelling slope currents: A numerical study. *J. Phys. Oceanogr.*, **29**, 1723–1743, https://doi.org/10.1175/1520-0485(1999)029<1723:WFDSCA>2.0.CO;2.

Nakayama, Y., M. Schröder, and H. H. Hellmer, 2013: From circumpolar deep water to the glacial meltwater plume on the eastern Amundsen Sea shelf. *Deep-Sea Res. I*, **77**, 50–62, https://doi.org/10.1016/j.dsr.2013.04.001.

——, R. Timmermann, M. Schröder, and H. Hellmer, 2014: On the difficulty of modeling Circumpolar Deep Water intrusions onto the Amundsen Sea continental shelf. *Ocean Modell.*, **84**, 26–34, https://doi.org/10.1016/j.ocemod.2014.09.007.

——, D. Menemenlis, H. Zhang, M. Schodlok, and E. Rignot, 2018: Origin of Circumpolar Deep Water intruding onto the Amundsen and Bellingshausen Sea continental shelves. *Nat. Commun.*, **9**, 3403, https://doi.org/10.1038/s41467-018-05813-1.

Naveira Garabato, A. C., and Coauthors, 2017: Vigorous lateral export of the meltwater outflow from beneath an Antarctic ice shelf. *Nature*, **542**, 219, https://doi.org/10.1038/nature20825.

Nuñez-Riboni, I., and E. Fahrbach, 2009: Seasonal variability of the Antarctic Coastal Current and its driving mechanisms in the Weddell Sea. *Deep-Sea Res. I*, **56**, 1927–1941, https://doi.org/10.1016/j.dsr.2009.06.005.

Orsi, A. H., T. Whitworth III, and W. D. Nowlin Jr., 1995: On the meridional extent and fronts of the Antarctic Circumpolar Current. *Deep-Sea Res. I*, **42**, 641–673, https://doi.org/10.1016/0967-0637(95)00021-W.

Paloczy, A., S. T. Gille, and J. L. McClean, 2018: Oceanic heat delivery to the Antarctic continental shelf: Large-scale,

low-frequency variability. *J. Geophys. Res. Oceans*, **123**, 7678–7701, https://doi.org/10.1029/2018JC014345.

Paolo, F. S., H. A. Fricker, and L. Padman, 2015: Volume loss from Antarctic ice shelves is accelerating. *Science*, **348**, 327–331, https://doi.org/10.1126/science.aaa0940.

Pritchard, H. D., S. R. M. Ligtenberg, H. A. Fricker, D. G. Vaughan, M. R. van den Broeke, and L. Padman, 2012: Antarctic ice-sheet loss driven by basal melting of ice shelves. *Nature*, **484**, 502–505, https://doi.org/10.1038/nature10968.

Rodriguez, A. R., M. R. Mazloff, and S. T. Gille, 2016: An oceanic heat transport pathway to the Amundsen Sea Embayment. *J. Geophys. Res. Oceans*, **121**, 3337–3349, https://doi.org/10.1002/2015JC011402.

Rossi, V., Y. Morel, and V. Garçon, 2010: Effect of the wind on the shelf dynamics: Formation of a secondary upwelling along the continental margin. *Ocean Modell.*, **31**, 51–79, https://doi.org/10.1016/j.ocemod.2009.10.002.

Ruan, X., A. F. Thompson, M. M. Flexas, and J. Sprintall, 2017: Contribution of topographically generated submesoscale turbulence to Southern Ocean overturning. *Nat. Geosci.*, **10**, 840–845, https://doi.org/10.1038/ngeo3053.

Schodlok, M. P., D. Menemenlis, E. Rignot, and M. Studinger, 2012: Sensitivity of the ice-shelf/ocean system to the sub-ice-shelf cavity shale measured by NASA IceBridge in Pine Island Glacier, West Antarctica. *Ann. Glaciol.*, **53**, 156–162, https://doi.org/10.3189/2012AoG60A073.

Shepherd, A., and Coauthors, 2018: Mass balance of the Antarctic Ice Sheet from 1992 to 2017. *Nature*, **558**, 219–222, https://doi.org/10.1038/s41586-018-0179-y.

Silvano, A., S. R. Rintoul, K. Kusahara, B. Peña-Molino, E. van Wijk, D. E. Gwyther, and G. D. Williams, 2019: Seasonality of warm water intrusions onto the continental shelf near the Totten Glacier. *J. Geophys. Res. Oceans*, **124**, 4272–4289, https://doi.org/10.1029/2018JC014634.

Smedsrud, L. H., A. Jenkins, D. M. Holland, and O. A. Nøst, 2006: Modeling ocean processes below Fimbulisen, Antarctica. *J. Geophys. Res.*, **111**, C01007, https://doi.org/10.1029/2005JC002915.

Spence, P., S. M. Griffies, M. H. England, A. M. C. Hogg, O. A. Saenko, and N. C. Jourdain, 2014: Rapid subsurface warming and circulation changes of Antarctic coastal waters by poleward shifting winds. *Geophys. Res. Lett.*, **41**, 4601–4610, https://doi.org/10.1002/2014GL060613.

——, R. M. Holmes, A. M. Hogg, S. M. Griffies, K. D. Stewart, and M. H. England, 2017: Localized rapid warming of West Antarctic subsurface waters by remote winds. *Nat. Climate Change*, **7**, 595–603, https://doi.org/10.1038/nclimate3335.

St-Laurent, P., J. M. Klinck, and M. S. Dinniman, 2013: On the role of coastal troughs in the circulation of Warm Circumpolar Deep Water on Antarctic Shelves. *J. Phys. Oceanogr.*, **43**, 51–64, https://doi.org/10.1175/JPO-D-11-0237.1.

——, ——, and ——, 2015: Impact of local winter cooling on the melt of Pine Island Glacier, Antarctica. *J. Geophys. Res. Oceans*, **120**, 6718–6732, https://doi.org/10.1002/2015JC010709.

Steig, E. J., Q. Ding, D. S. Battisti, and A. Jenkins, 2012: Tropical forcing of Circumpolar Deep Water inflow and outlet glacier thinning in the Amundsen Sea Embayment, West Antarctica. *Ann. Glaciol.*, **53**, 19–28, https://doi.org/10.3189/2012AoG60A110.

Stewart, A. L., A. Klocker, and D. Menemenlis, 2018: Circum-Antarctic shoreward heat transport derived from an eddy- and tide-resolving simulation. *Geophys. Res. Lett.*, **45**, 834–845, https://doi.org/10.1002/2017GL075677.

Thoma, M., A. Jenkins, D. Holland, and S. Jacobs, 2008: Modelling Circumpolar Deep Water intrusions on the Amundsen Sea continental shelf, Antarctica. *Geophys. Res. Lett.*, **35**, L18602, https://doi.org/10.1029/2008GL034939.

Thompson, A. F., K. J. Heywood, S. Schmidtko, and A. L. Stewart, 2014: Eddy transport as a key component of the Antarctic overturning circulation. *Nat. Geosci.*, **7**, 879–884, https://doi.org/10.1038/ngeo2289.

Thomson, W. J., and R. E. Emery, 2014: *Data Analysis Methods in Physical Oceanography.* 3rd ed. Elsevier Science, 728 pp.

Timmermann, R., and Coauthors, 2010: A consistent data set of Antarctic ice sheet topography, cavity geometry, and global bathymetry. *Earth Syst. Sci. Data*, **2**, 261–273, https://doi.org/10.5194/essd-2-261-2010.

Wåhlin, A. K., X. Yuan, G. Björk, and C. Nohr, 2010: Inflow of warm Circumpolar Deep Water in the central Amundsen shelf. *J. Phys. Oceanogr.*, **40**, 1427–1434, https://doi.org/10.1175/2010JPO4431.1.

——, R. D. Muench, L. Arneborg, G. Björk, H. K. Ha, S. H. Lee, and H. Alsén, 2012: Some implications of Ekman layer dynamics for cross-shelf exchange in the Amundsen Sea. *J. Phys. Oceanogr.*, **42**, 1461–1474, https://doi.org/10.1175/JPO-D-11-041.1.

——, and Coauthors, 2013: Variability of warm deep water inflow in a submarine trough on the Amundsen shelf. *J. Phys. Oceanogr.*, **43**, 2054–2070, https://doi.org/10.1175/JPO-D-12-0157.1.

Walker, D. P., M. A. Brandon, A. Jenkins, J. T. Allen, J. A. Dowdeswell, and J. Evans, 2007: Oceanic heat transport onto the Amundsen Sea shelf through a submarine glacial trough. *Geophys. Res. Lett.*, **34**, L02602, https://doi.org/10.1029/2006GL028154.

——, A. Jenkins, K. M. Assmann, D. R. Shoosmith, and M. A. Brandon, 2013: Oceanographic observations at the shelf break of the Amundsen Sea. *J. Geophys. Res. Oceans*, **118**, 2906–2918, https://doi.org/10.1002/jgrc.20212.

Wallace, J. M., C. Smith, and C. S. Bretherton, 1992: Singular value decomposition of wintertime sea surface temperature and 500-mb height anomalies. *J. Climate*, **5**, 561–576, https://doi.org/10.1175/1520-0442(1992)005<0561:SVDOWS>2.0.CO;2.

Webb, D. J., R. M. Holmes, P. Spence, and M. H. England, 2019: Barotropic Kelvin wave-induced bottom boundary layer warming along the West Antarctic Peninsula. *J. Geophys. Res. Oceans*, **124**, 1595–1615, https://doi.org/10.1029/2018JC014227.

Webber, B. G., and Coauthors, 2017: Mechanisms driving variability in the ocean forcing of Pine Island Glacier. *Nat. Commun.*, **8**, 14507, https://doi.org/10.1038/ncomms14507.

——, K. J. Heywood, D. P. Stevens, and K. M. Assmann, 2019: The impact of overturning and horizontal circulation in Pine Island trough on ice shelf melt in the Eastern Amundsen Sea. *J. Phys. Oceanogr.*, **49**, 63–83, https://doi.org/10.1175/JPO-D-17-0213.1.